Blazed 3D Cells with Application to Full-Metal Dichroic Mirrors

Charalampos Stoumpos, Lucas Polo-López, Hervé Legay, Thierry Pierré, M. García-Vigueras

Blazed 3D Cells with Application to Full-Metal Dichroic Mirrors

Charalampos Stoumpos, Lucas Polo-López, Hervé Legay, Thierry Pierré and María García-Vigueras, *Member, IEEE*

***Abstract*—A novel frequency selective surface (FSS) architecture for dichroic mirrors is presented in this work. The solution employs a full-metal unit cell which was conceived as the transmission equivalent of the blazed grating opaque metallic structures operating in retrodirective reflection. The unit cell is based on a transverse electro-magnetic (TEM) topology, while basic filter analysis for a bandpass response has also been employed. This TEM topology brings significant reduction of the 3-D cell's periodicity allowing operation in the subwavelength regime so that grating lobes are avoided. This, in turn, brings enhanced angular stability in terms of amplitude and phase transmission for both TE and TM incidence. The principal application of the proposed dichroic mirror relates to the Deep Space Antenna. Owing to the blazed grating concept, the unit cell was optimized for an incident elevation angle of θ=30°. The blazed architecture, the filtering synthesis, design details towards a 3D-printing compatible solution as well as equivalent circuit analysis of the unit cell are described in detail. Numerical results show that the proposed solution exhibits a very robust RF performance. The characterized reflection coefficient remains below -10 dB, the Cross-Polarization Discrimination (XPD) above 16.5 dB, the low-band (i.e., 0.4f_0) rejection below -26 dB and the transmission losses below 0.5 dB for both TE and TM incidence over a wide frequency bandwidth (≈25%) and angular range (0°≤ θ≤40°). The simulation results of a linearly polarized horn that illuminates the proposed dichroic mirror have been verified by measurements which included two prototypes fabricated in Selective Laser Melting (SLM) using aluminum alloy. In light of the favorable performance, the proposed solution constitutes an appealing candidate for dichroic mirrors of Deep Space missions.**

***Index Terms*—3-D periodic structures, 3-D Printing, Additive Manufacturing, Blazed Unit Cell, Deep Space Antenna, Dichroic Mirror, Equivalent Circuit, Frequency Selective Surface (FSS), Parallel Plate Waveguide (PPW), Selective Laser Melting (SLM), Spatial Filter.**

Manuscript received September 11, 2023; revised February 17 and July 5, 2024; accepted Month Day, 2024. This work was supported by the Key Technology Domain (KTD) research and innovation program between Thales Alenia Space and INSA Rennes.

C. Stoumpos, L. Polo-López and María García-Vigueras are with the Institute d'Electronique et Télécommunications de Rennes, UMR CNRS 6164, INSA de Rennes, Rennes (e-mail: charalampos.stoumpos@insa-rennes.fr, haris_stou@hotmail.com, lucas.polo-lopez@insa-rennes.fr, maria.garcia-vigueras@insa-rennes.fr).

H. Legay and T. Pierré are with the Department of Research and Technology, Thales Alenia Space, 31037 Toulouse, France. (e-mail: herve.legay@thalesaleniaspace.com, thierry.pierre@thalesaleniaspace.com)

Color versions of one or more figures in this article are available at https://doi.org/xx.xxxx/TAP.202x.xxxxxxx.

Digital Object Identifier xx.xxxx/TAP.202x.xxxxxxx

I. Introduction

Frequency Selective Surfaces are widely used in various microwave applications [1]. Among many implementations, FSS, can be used as spatial filters providing lowpass, bandpass, highpass and bandstop frequency responses. In contrast, however, to microwave filters [2], the polarization of the electric field and the angle of incidence affect their frequency response.

The concept of blazed (or echelette) grating is a subgroup of diffraction grating optimized to achieve maximum efficiency in a given diffraction order [3]. Therefore, maximum power focuses on the selected diffraction order while the residual power in the other orders is minimized. As a result, unlike mirrors and metallic plates that only reflect specular waves, blazed gratings can reflect an oblique incident wave back in the path of incidence (retrodirective reflection). A special condition refers to the so-called Littrow configuration, where the blaze angle is chosen such that diffraction angle and incidence angle are identical.

Blazed gratings are typically used in optics in order to manipulate the phase, amplitude and polarization of light [4]. They find application in various domains such as pulse compression in ultrafast optics [5], lenses for imaging [6], sub-optical resonators for coupling mirrors [7], as well as optical multiplexers [8] or filters [9]. Blazed gratings operating in the microwave ranges have been implemented on corrugated metallic surfaces [10] and on planar metasurfaces mimicking the classical non-planar sawtooth gratings [11]-[12].

Fig. 1(a) depicts a typical planar FSS structure operating in transmission (within the bandpass response) and normal incidence (i.e., θ_i = 0°). Fig. 2(b) shows the classical sawtooth grating operating under the Littrow condition (i.e., θ_i = θ_0 = blaze angle). Inspired by these two abovementioned concepts, this work adopts and combines the blazed architecture depicted in Fig. 1(b) with the spatial filtering FSS function in Fig. 1(a). This results in the development of an innovative metallic dichroic mirror topology, the basic operational principle of which is depicted in Fig. 1(c). It could be in fact interpreted as the transmission equivalent of the metallic (and therefore reflecting) sawtooth grating in Fig. 1(b).

One of the applications of FSS is their employment as dichroic mirrors [13]-[14]. In Deep Space applications, the dichroic mirrors must satisfy tight electrical and mechanical specifications [15]. In particular, the screen operates in dual-

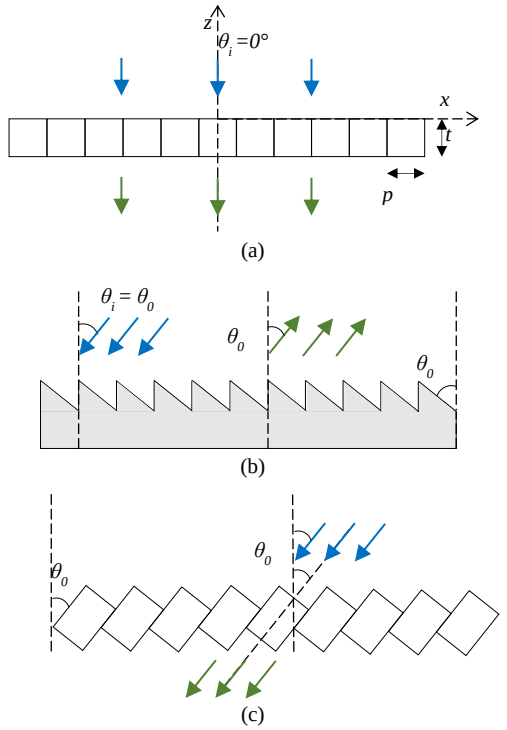

Fig. 1. Principal concept of dichroic mirrors based on 3D blazed cells: (a) typical FSS illuminated from broadside (θ_i=0°) with flat surfaces in x=0 (input) and x=t (output) operating in transmission, (b) typical blazed grating illuminated from θ_i>0° operating in reflection (sawtooth or echellette interface at input) and (c) proposed FSS with blazed grating square cells illuminated from θ_i>0° operating in transmission (sawtooth or echellette interface at input and output).

circular polarization (dual-CP) and acts as a high-pass spatial filter; namely, it reflects completely in the lower band and presents minimum insertion loss in the lower band (typically two sub-bands for the uplink and the downlink). Moreover, unlikely the typical FSS considerations, the cross-polar discrimination (XPD) must be high enough (typically above 20 dB) so that the performance of the overall antenna system is maintained.

In addition, dichroic mirrors are typically illuminated by a corrugated horn in oblique incidence. In Deep Space applications, the nominal incidence angle is 30°. Nevertheless, the horn's radiation does not relate to an ideal uniform plane wave (tapered illumination). The analysis of the dichroic mirror is typically performed under the hypothesis of an approach based on the expansion of the field generated by the source into a discrete set of uniform plane waves [16]. In this case, the consideration of only the plane wave with the nominal angle of incidence is not a sufficient approximation and, therefore, other spectral components of the illuminating beam (i.e., plane waves traveling in different directions) must be taken into account [17]. Given the fact that around 60% of the illuminating source's energy (i.e., the horn antenna feed's illumination tapering) impinges on the central part of the dichroic mirror, a tolerable performance can be achieved for an optimization around 30°±5° [16]. Nevertheless, the overall electrical performance of the dichroic mirror should ideally be optimized for a significantly larger number of incident angles; typically, the angular range is of the order of θ = 30°±15° [17]. There are two principal figures of merit related to the electrical performance of dichroic mirrors; the reflection level (considering also the ohmic losses) as well as the XPD over the afore-mentioned angular range.

Dichroic mirrors for Deep Space applications should be full-metal structures due to the required power-handling [18]. Therefore, due to the high power levels, such applications should also involve minimized losses, planar dielectric-based FSS solutions are prohibitive (low power-handling and dielectric losses). The state-of-the-art dichroic mirror solutions for Deep Space applications relate to the seminal concept of a metallic mesh in far infrared spectroscopy [19]. This concept was later analyzed and formulated as a general solution to the determination of the aperture field distribution and then the transmission and reflection coefficients of an infinite planar conducting sheet perforated periodically with apertures [20]-[21]. Considering an arbitrary angle plane wave incident excitation, the aperture dimensions and array element spacings are of the order of the wavelength of the incident electromagnetic field.

As a result, current practice relies on the optimization of the above concept of a perforated metallic plate for the development of efficient dichroic mirrors for Deep Space applications. Several design approximations and optimization strategies have been proposed in the literature and constitute the state-of-the-art [15], [18], [22]-[23].

The current operational frequencies of deep-space antennas allocated by the International Telecommunication Union (ITU) for both uplink and downlink are S-band (2.025 – 2.3 GHz), X-band (7.145 – 8.5 GHz), K-band (22.5 – 27 GHz) and Ka-band (31.8 – 34.7 GHz) [13]-[17]. Both dual-band [15], [23] (the mirror D2) and full-band [14], [18], [23] (the mirror D1) designs have been addressed so far in the literature in order to fulfil the bandwidth requirements. These are of the order of up to 20% of fractional bandwidth when, furthermore, considering the afore-mentioned angular range of θ = 30°±15° which relates to the illumination of the CP horn on the dichroic mirror as well.

Upcoming and planed missions to the Moon and beyond have already demonstrated the need for an uplink channel significantly larger in frequency bandwidth than those typically used in S- and X-bands [23]. The current requirements in K-band call for a frequency bandwidth of the order of up to 20% (22.5 – 27 GHz), while future trends may even exceed these bandwidth requirements as well as include more frequency bands other than the already allocated ones and geometrical configurations in terms of focal point and dimensions of dichroic mirrors.

Three-dimensional (3-D) FSS have been studied over the past years as they prove to exhibit superior performance compared to conventional two-dimensional (2-D) ones [24]-[33]. Nowadays, additive manufacturing allows to realize structures in a cost- and performance-efficient fashion, which otherwise would be more complicated, if not impossible, to do through conventional manufacturing techniques [34]. In this work, we exploit the fully metallic unit-cell that supports

transverse electromagnetic (TEM) modes [33], as it is easily adapted to the blazed topology, while it is also enabled through 3D-printing. This cell was initially employed for the development of polarizing screens using aluminum SLM and presents inherently broad bandwidth as it is the equivalent of parallel plate waveguides (PPW) for periodic structures. In addition, it is well established that 3D-printed surfaces present a superior power-handling level with reference to machined ones [35]. This aspect is of great significance for Deep Space applications.

An equally critical aspect for the design of FSS or polarizers is their angular stability. In particular, the cells of a periodic structure should respect the critical grating lobe limit of half wavelength or in other words they should present subwavelength periodicity. This assures the suppression of higher order Floquet harmonics and hence grating lobes over a wide angular range of incidence. It is well established that this condition is achieved through miniaturization which has been an important subject of research over the past decades [36]-[41]. In this work, the miniaturization is enabled by the TEM 3D-cell used for the design of the presented dichroic mirror. Moreover, by loading the cell with innovative 3D reactive elements it is possible to synthesize inductive and capacitive impedances connected in parallel within the TEM line, and thus, to create a wide bandpass response in a cell with subwavelength periodicity [42].

The design is generic, and all dimensions are given as a function of the free-space wavelength λ_0, corresponding to the central frequency of the specified bandwidth. The proposed dichroic mirror has been engineered through Selective Laser Melting (SLM) using aluminum alloy in order to verify the simulations and prove the concepts of this work. The prototypes have been designed at f_0 = 15GHz with view to explore the fabrication potentiality in the demanding Ku-band as well as for reasons of compatibility with our measurement setup which includes a horn antenna, a polymer positioning structure for the dichroic mirror and a compact range anechoic chamber operating from 0.6 to 18 GHz.

The paper is structured as follows. Section II describes the topology of the original unit cell and its behavior. These relate to the progressive construction of the cell based on a TEM unit cell that is loaded with 3D inductive or capacitive elements. Such 3D elements allow synthesizing resonances, and thus, a passband response. The benefits of the blazing of this cell are here considered. The conception of the cell is justified progressively with simple equivalent circuit models that are systematically validated with full-wave solvers. Such an analysis allows to tune thoroughly the operation of the unit cell. Section III describes the adaptations of the rigorous mechanical and RF co-design and optimization of the final unit cell. Section IV provides the associated fabrication strategy of the total dichroic mirror followed so that the additive manufacturing rules are respected, the experimental verification of the presented concept through measurements of a 3D-printed prototype illuminated by a linearly polarized (LP) standard gain horn antenna as well as a discussion on the measurement results related to deviations that were observed in terms of the frequency shift between simulations and measurements. Finally, section V presents the conclusions of this work.

II. Description of the Unit Cell and its Evolution

The E-field of a time-harmonic circular-polarized (CP) impinging wave propagating in the +z-direction can be expressed by its two orthogonal components, TE and TM, as follows:

$$\mathbf{E}^i_{\mathrm{LHCP}} = \frac{1}{\sqrt{2}}\left(\mathbf{E}^i_{\mathrm{TE}} + j\mathbf{E}^i_{\mathrm{TM}}\right) \tag{1a}$$

$$\mathbf{E}^i_{\mathrm{RHCP}} = \frac{1}{\sqrt{2}}\left(\mathbf{E}^i_{\mathrm{TE}} - j\mathbf{E}^i_{\mathrm{TM}}\right) \tag{1b}$$

with

$$\mathbf{E}^i_{\mathrm{TE}} = \mathrm{E}^i_0\, e^{j(\omega t - \mathrm{k}_0 z)}\,\hat{\mathrm{y}} \tag{2a}$$

$$\mathbf{E}^i_{\mathrm{TM}} = \mathrm{E}^i_0\, e^{j(\omega t - \mathrm{k}_0 z)}\,\hat{\mathrm{x}} \tag{2b}$$

where E_0 is the amplitude of the field and k_0 is the free-space wavenumber. The superscript *i* refers to incidence. From eq. (1) it is denoted that the phase difference between TE and TM incidence for an E-field in LHCP and RHCP impinging on the dichroic mirror is: $\Delta\varphi^i = \varphi^i_{\mathrm{TE}} - \varphi^i_{\mathrm{TM}} = \pm 90°$.

The performance of the mirror in terms of CP-purity is dictated after the evaluation of the transmitted E-field through the mirror. We therefore decompose the transmitted E-field into its two orthogonal and linearly polarized transmitted TE and TM components as:

$$\mathbf{E}^t_{\mathrm{TE}} = \mathrm{E}^t_{0,\,\mathrm{TE}}\, e^{j(\omega t - \mathrm{k}_0 z + \varphi^t_{\mathrm{TE}})}\hat{\mathrm{y}} \tag{3a}$$

$$\mathbf{E}^t_{\mathrm{TM}} = \mathrm{E}^t_{0,\,\mathrm{TM}}\, e^{j(\omega t - \mathrm{k}_0 z + \varphi^t_{\mathrm{TM}})}\hat{\mathrm{x}} \tag{3b}$$

A dichroic mirror which presents ideal CP-purity should have no impact on the amplitude and phase difference of the two incident, orthogonal and linearly polarized components $\mathbf{E}^i_{\mathrm{TE}}$ and $\mathbf{E}^i_{\mathrm{TM}}$, which compose the total incident E-field referring to equations (1) and (2). In other words, an ideal dichroic mirror should respect the conditions: $\mathbf{E}^i_{\mathrm{TE}} = \mathbf{E}^t_{\mathrm{TE}}$, $\mathbf{E}^i_{\mathrm{TM}} = \mathbf{E}^t_{\mathrm{TM}}$, $\Delta\varphi^i = \varphi^i_{\mathrm{TE}} - \varphi^i_{\mathrm{TM}} = \pm 90°$ and $\Delta\varphi^t = \varphi^t_{\mathrm{TE}} - \varphi^t_{\mathrm{TM}} = \pm 90°$ for an E-field in LHCP and RHCP impinging on the mirror (index *i*) and transmitted by the mirror (index *t*).

So, the transmission coefficient (or insertion gain) of an y-polarized (x-polarized) wave transmitted through the mirror is defined as $\mathrm{E}^t_{0,\,\mathrm{TE}}/\mathrm{E}^i_0$ ($\mathrm{E}^t_{0,\,\mathrm{TM}}/\mathrm{E}^i_0$), while the degradation level of the phase difference between the two orthogonal components of the E-field after its transmission from the mirror is described as:

$$\Delta\varphi^{error} = \left|\Delta\varphi^t - \Delta\varphi^i\right| \tag{4}$$

A dichroic mirror which presents ideal CP-purity will give:

$\Delta\varphi^{error} = 0$. Considering all the above, we can finally define the typical figure of merits for the evaluation of a CP field, which are the Cross-Polarized Discrimination (XPD) and the Axial Ratio (AR) [43]:

$$\mathrm{XPD}_{[\mathrm{dB}]} = 20\log\left(\frac{\mathrm{AR}+1}{\mathrm{AR}-1}\right) \tag{5}$$

$$\mathrm{AR} = \frac{\sqrt{\left|\mathrm{E}^t_{0,\,\mathrm{TE}}\right|^2 + \left|\mathrm{E}^t_{0,\,\mathrm{TM}}\right|^2 + \sqrt{\mathrm{a}}}}{\sqrt{\left|\mathrm{E}^t_{0,\,\mathrm{TE}}\right|^2 + \left|\mathrm{E}^t_{0,\,\mathrm{TM}}\right|^2 - \sqrt{\mathrm{a}}}} \tag{6}$$

$$\mathrm{a} = \left|\mathrm{E}^t_{0,\,\mathrm{TE}}\right|^4 + \left|\mathrm{E}^t_{0,\,\mathrm{TM}}\right|^4 + 2\left|\mathrm{E}^t_{0,\,\mathrm{TE}}\right|^2\left|\mathrm{E}^t_{0,\,\mathrm{TM}}\right|^2\cos(2\Delta\varphi) \tag{7}$$

$$\Delta\varphi = 90° \pm \Delta\varphi^{error} \tag{8}$$

The unit cell is based on the seminal TEM-based concept that was used for the development of polarizing screens and was first introduced in [33]. It employs lateral slits which emulate a PPW operation, presents large bandwidth thanks to the TEM-like propagation (no cutoff), dual polarization and can operate in subwavelength periodicity (3-D fully metallic meta-atom).

A. 1st Order Unit Cell

The design methodology commences with the insertion of a reactive inductive load in the middle of the unit cell's longitudinal profile. First, through full-wave EM simulations, we characterize the impedance of the unloaded unit cell in order to design the equivalent circuit of the loaded topology. The geometry of the loaded unit cell is shown in Fig. 2(a). An X-shape load is here considered. This is physically represented by two orthogonal metallic bars connected to the four angles formed by the lateral slitted metallic walls of the unit cell. This load acts as a parallel inductance (L) as shown in Fig. 2(b). The analysis of the input impedance as a function of the unit cell's geometrical characteristics (i.e., p, d, w_x, w_y) has already been presented in [33] and therefore is omitted for sake of simplicity. Similarly, as per [33], by varying the diameter of the load's metallic bars we can vary the value of the inductance; smaller diameter values give larger inductance and vice versa. In the rest, the bandpass response is obtained by tuning the three degrees of freedom of the equivalent circuit, namely Z_1, d_c and L.

The response of this 1st order unit cell is depicted in Fig. 2(c). The reflection coefficient remains below -10 dB over a fractional bandwidth of around 40%. It is observed that the equivalent circuit's response agrees totally with that of the full-wave simulation. On one hand, the equivalent circuit does not include dynamic multimodal effects for the sake of simplicity. On the other hand, the unit cell presents subwavelength periodicity ($p \approx 0.27\lambda_0$, where λ_0 is the wavelength at the central frequency) and therefore the higher order Floquet modes are well below cutoff over the operating frequency bandwidth. This leads to a highly reactive unit cell with a quasi-static behavior and as a result its full-wave analysis shows high agreement with the one of its equivalent circuit.

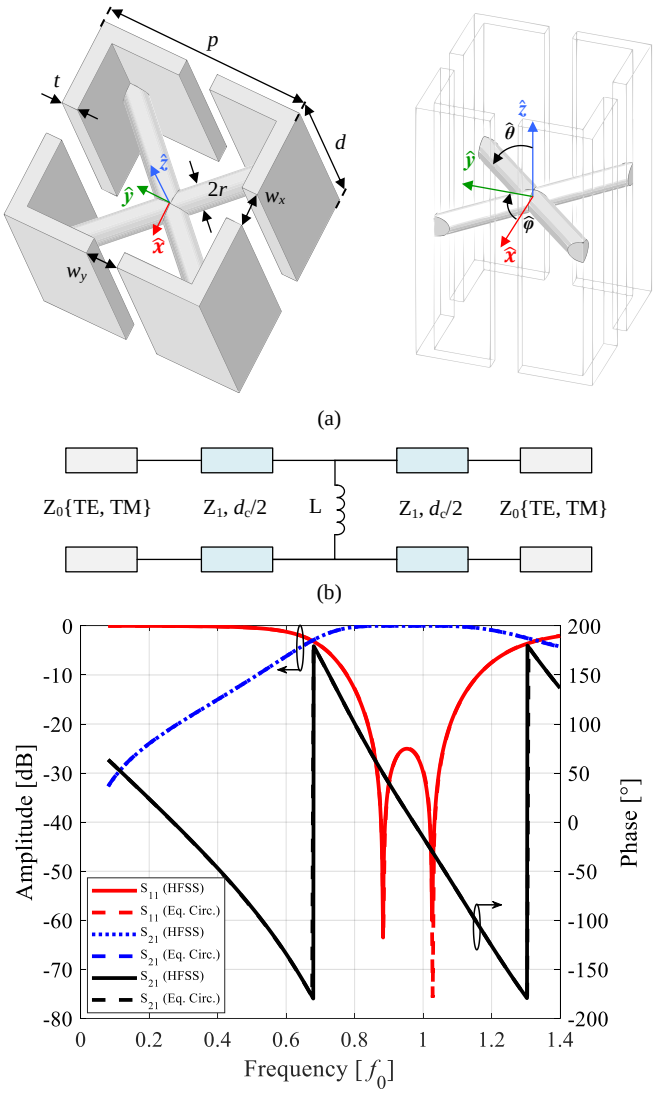

Fig. 2. The 1st order TEM unit cell: (a) layout and geometrical parameters (p=0.265λ_0, d=0.417λ_0, t=0.021λ_0, r=0.017λ_0, w_x=w_y=0.042λ_0), (b) proposed equivalent circuit and (c) calculated S-parameters for an incident angle of {φ=0°, θ=0°}, TE and TM incidence (identical in this case) and equivalent circuit values of: Z_0≈376.73 Ω, Z_1=125 Ω, d_c=0.43λ_0, L=0.341 nH.

The thickness of the unit cell is slightly different between the full-wave model (d) and equivalent circuit (d_c), with the former being smaller of the latter (i.e., for θ=0°, d=0.417λ_0 < d_c=0.43λ_0). This is attributed to the fact that the full-wave (CAD) model employs physical loads with specific geometry (i.e., the parameter r in the case of the X-shape inductive load), while the equivalent circuit employs lumped elements with non-physical geometry and volume.

Fig. 3 depicts the S-parameters of the unit cell from Fig. 2(a) for different angles of incidence (θ). The reflection coefficient for both TE [Fig. 3(a)] and TM [Fig. 3(b)] remains below -10 dB over a fractional bandwidth of 25% for incidence up to θ=40°. This, together with the agreement of the equivalent circuit's response with the full-wave simulations, are again attributed to the miniaturized footprint of the unit cell. The values of the equivalent circuit's components are given in

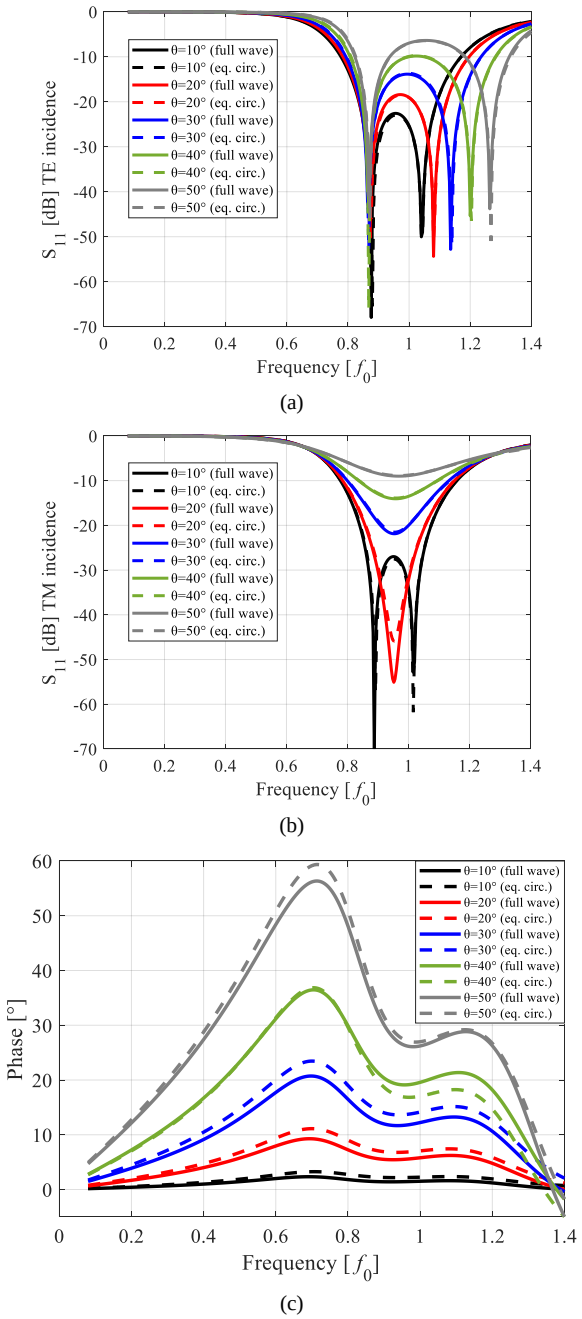

Fig. 3. Performance of the 1st order TEM unit cell from Fig. 1(a) as a function of the incident angle θ: (a) reflection coefficient (S_{11}) for TE incidence (E_y component), (b) reflection coefficient for TM incidence (E_x component) and (c) phase difference between the TE and TM transmission coefficients. The equivalent circuit's values [Fig. 1(b)] can be found in Table I.

TABLE I
EQUIVALENT CIRCUIT VALUES OF THE 1ST ORDER UNIT CELL (FIG. 2A)

	d_c [λ_0]	L [nH]
θ=10°, TE	0.4275	0.339
θ=10°, TM	0.431	0.342
θ=20°, TE	0.42	0.334
θ=20°, TM	0.432	0.342
θ=30°, TE	0.408	0.33
θ=30°, TM	0.4325	0.343
θ=40°, TE	0.395	0.322
θ=40°, TM	0.435	0.344
θ=50°, TE	0.382	0.315
θ=50°, TM	0.44	0.345

Table I, where $Z_{0,TE} = Z_0/\cos(\theta)$, $Z_{0,TM} = Z_0 \cdot \cos(\theta)$, $Z_0 = \sqrt{\frac{\mu_0}{\varepsilon_0}} \approx 376.73\ \Omega$ and $Z_{1,TE} = Z_{1,TM} = 125\ \Omega$, $\forall\ \theta$.

Owing to the design's symmetry in both transversal planes (i.e., xz and yz), the input impedance of the equivalent circuit is fixed (i.e., Z_1=125 Ω) for all incident angles (θ=0°, 10°, …, 50°) and both TE and TM incidence. The inductance values (L) present negligible variations as a function of the incident angle as well (i.e., from 0.315 to 0.345 nH). Fig. 3(c) depicts the phase difference between the TE and TM transmission coefficients. It is shown that for incidence greater than 30°, the phase imbalance gets values above 10°. This means that the XPD will decrease significantly for θ>30°.

B. 1st Order Blazed Unit Cell

From section II.A, it was identified that the first problematic aspect of the basic 3-D unit cell in Fig. 2(a) relates to the decreased XPD for incidence greater than 30°. Considering also that the principal application relates to the Deep Space Antenna, high XPD for incidence angles in the range 30°±15° is a key requirement.

Fig. 4(a) depicts the blazed grating geometry of the 1st order unit cell. This is the same unit cell of Fig. 2(a) which is tilted along y-axis with a blaze angle a. Fig. 4(b) shows a 3×3 array of this unit cell in perspective view, which is the 3D equivalent of the concept illustrated in Fig. 1(c).

Figures 5(a) to 5(d) show the simulated (full-wave and equivalent circuit) S-parameters of the unit cell from Fig. 4(a) for a blaze angle of a=30°, different angles of incidence (θ=0°, 10°, …, 50°) as well as TE and TM incidence. The equivalent circuit employed is the one of Fig. 2(b) and its values are given in Table II. In the case of this equivalent circuit analysis and as a comparison to the initial non-blazed case, the input impedance values (Z_1) are not the same for TE and TM incidence. We can see that for TE incidence, Z_1 varies around 147 Ω with values of ±5 Ω as a function of the incidence angle (θ), while for TM incidence, around 110 Ω with values of ±2 Ω as a function of the incidence angle (θ). A similar differentiation for TE and TM incidence is also observed for the inductance values (L) of the equivalent circuit. As a function of the incident angle (θ), the inductance varies from 0.386 to 0.413 nH and 0.3 to 0.31 nH for TE and TM incidence, respectively. These differentiations are attributed to

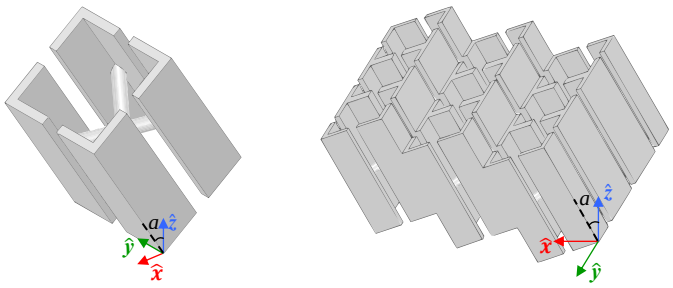

Fig. 4. The inclined (blazed) 1st order TEM unit cell: (a) layout of the unit cell [a = 30° and the rest geometrical parameters are the same as Fig.1(a)] and (b) a 3×3 array example which employs the inclined unit cell.

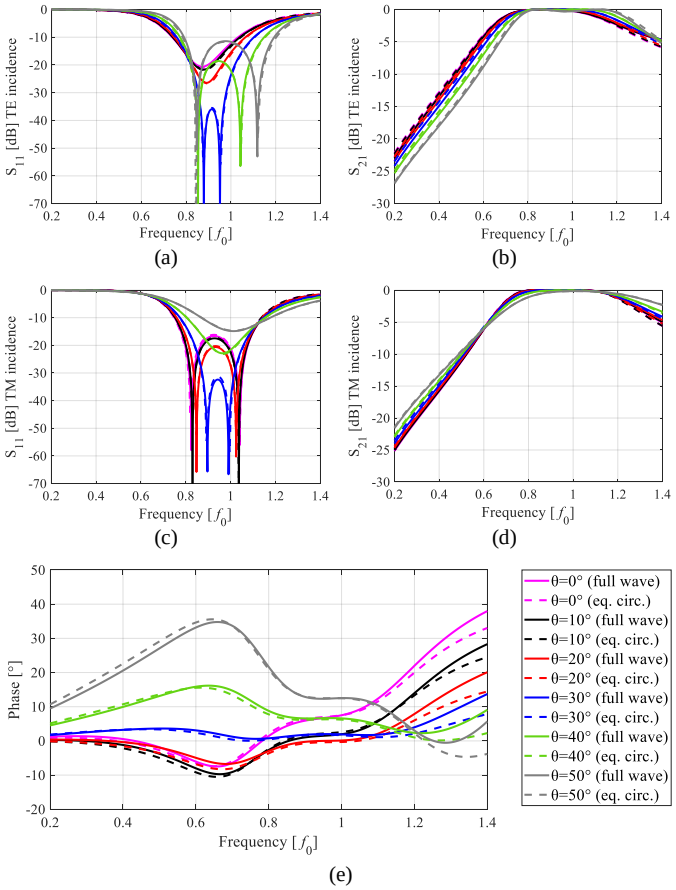

Fig. 5. Full-wave and equivalent circuit simulation results of the 1st order blazed unit cell for different incident angles (θ): (a) TE reflection coefficient, (b) TE transmission coefficient, (c) TM reflection coefficient, (d) TM transmission coefficient and (e) phase difference ($\Delta\varphi^{error}$) between the TE and TM transmission coefficients. The equivalent circuit's values [Fig. 1(b)] are in Table II [$Z_{0,TE} = Z_0/\cos(\theta)$, $Z_{0,TM} = Z_0 \cdot \cos(\theta)$, $Z_0 \approx 376.73\ \Omega$].

the fact that the inclination of the cell (i.e., blazing) induces an asymmetry between the two transversal (xz- and xy-) planes.

As a result, a plane wave impinging on a FSS comprising such blazed cells will no longer experience the same periodicity and geometry for both xz- and xy-planes, or else, for both TE and TM incidence. This breaking of the unit cell's symmetry is substantially the key factor for the improvement of the cell's performance in terms of S-parameters, as well as, most importantly, the minimization of the phase difference

TABLE II
EQUIVALENT CIRCUIT VALUES OF THE 1ST ORDER BLAZED UNIT CELL
(FIG. 4)

	Z_1 [Ω]	d_c [λ_0]	L [nH]
θ=0°, TE	142	0.469	0.413
θ=0°, TM	112	0.438	0.31
θ=10°, TE	143	0.466	0.413
θ=10°, TM	111	0.438	0.302
θ=20°, TE	145	0.458	0.413
θ=20°, TM	111	0.436	0.303
θ=30°, TE	148	0.446	0.413
θ=30°, TM	112	0.431	0.311
θ=40°, TE	150	0.431	0.4
θ=40°, TM	110	0.423	0.302
θ=50°, TE	152	0.416	0.386
θ=50°, TM	108	0.405	0.3

($\Delta\varphi^{error}$) between the TE and TM transmission coefficients for oblique incidence, which in turn, reduces the XPD.

The reflection coefficient for both TE and TM incidences remains below -10 dB over a fractional bandwidth of around 26% for incidence up to θ=40°. Owing to the blazing concept and in contrast to the non-blazed case, it is observed that the reflection coefficient of the blazed unit cell remains below -10 dB over a fractional bandwidth of around 17% for incidence even up to θ=50°. This fact denotes that the inclination of the unit cell improves its reflection and transmission amplitude response for a slightly larger frequency bandwidth as well as more oblique incidence angles (θ) with respect to the non-blazed topology [see Figs. 3(a)-(b)]. On the other hand, Fig. 5(e) depicts the phase difference between the TE and TM transmission coefficients [($\Delta\varphi^{error}$) from eq. (4)], where it is clearly observed that the phase imbalance is almost eliminated. In particular, the phase difference between TE and TM transmission remains in the range of -2~9° over 0.8~1.04f_0 and for θ up to 40°. Regarding the case where the incidence angle is equal to the blaze angle ($\theta = a$ = 30°), this phase imbalance varies between 1~4° over 0.1~1.2f_0 [blue line in Fig. 5(c)]. This last observation proves to a high extent the benefit of the blazed grating concept.

As a matter of fact, the advantage of inclining the cell is better described in Fig. 6. This figure shows the phase difference between the TE and TM transmission coefficients [$\Delta\varphi^{error}$ from eq. (4)] for equal blaze (a) and incidence (θ) angles within an angular range of $0° \le a = \theta \le 50°$. The phase imbalance for all these cases varies between -1~4° at f_0. Assuming a zero power-imbalance between the two transmission coefficients of the two orthogonal modes, TE and TM, such a phase shift induces XPD values higher than 27 dB.

C. 3rd Order Blazed Unit Cell

Section II.B dealt with the phase imbalance elimination of the 1st order TEM unit cell between the TE and TM transmission coefficients introducing, thereby, the interest to follow the blazed grating concept. Numerical results showed that if the blaze and incidence angles are equal, this phase difference gets values close to zero and hence the XPD of a dichroic mirror composed of such cells can be maximized.

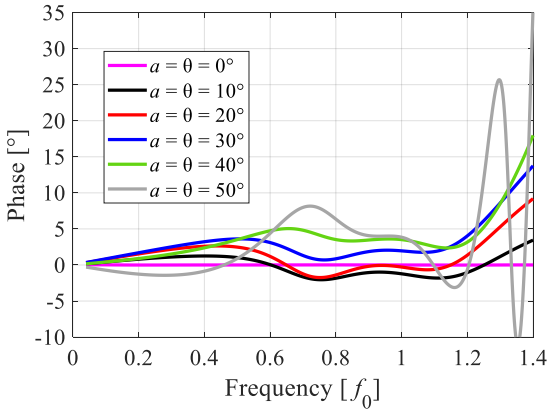

Fig. 6. Phase difference ($\Delta\varphi^{error}$) between the TE and TM transmission coefficients (S_{21}) for equal inclination (a) and incidence angles (θ) of the 1st order blazed unit cell in Fig. 4.

However, the unit cell should operate efficiently as a spatial high-pass filter as well. This means that for the lower frequencies, the unit-cell should exhibit a significant reflection level which will make it mimic a metallic mirror. Nevertheless, Figs. 5(b) and 5(d) show that the unit-cell does not exhibit a sufficiently high selectivity (i.e., S_{11}<-25 dB at least) over the specified roll-off (≈0.34f_0) for the Deep Space Antenna owing to the single inductive load employed.

The design of planar (2-D) band-pass FSS composed of non-resonant constituting elements is a well-established synthesis procedure [36]-[42]. In particular, it has been shown that by cascading bandpass surfaces in a proper fashion, any arbitrary multipole filter or non-commensurate multiband response can be obtained. This section introduces the concept and synthesis of a TEM unit-cell with a 3rd order bandpass frequency response in order to enhance the roll-off in the lower frequencies.

In this section, we present the application to 3-D full-metal unit cells of the seminal filter synthesis for FSS [42], realized in printed circuit technology using multiple stacked dielectric substrates. The concept is illustrated in Fig. 7(a), which shows a 3rd order TEM unit cell comprising three distinct elements in parallel connection along its profile. The topology is composed of two inductive loads similar to the ones used in sections II.A and II.B as well as a capacitive load between them. The capacitive load is represented by a floating metallic patch which is placed in an appropriate distance (d_2) between the two inductive loads so as to control the bandpass poles of this FSS which acts as a spatial filter. The area of the metallic patch (l_c×l_c) defines the value of the capacitance; larger areas give larger capacitance and vice versa. The bandpass response is obtained by tuning the five degrees of freedom of the equivalent circuit, namely Z_1, d_{1c}, d_{2c}, L and C. The periodicity of the unit-cell is sub-wavelength. Fig. 7(b) shows the equivalent circuit of this 3rd order TEM unit cell, where the components of the 3-D cell are represented in a circuit level and the 3rd order filtering arrangement is made obvious.

The response of this 3rd order filtering FSS is depicted in Fig. 7(c). The reflection coefficient remains below -10 dB over a fractional bandwidth of 35% (0.84~1.2f_0), while the transmission coefficient below 0.4f_0 (roll-off) is below -30 dB. The selectivity of the 3rd order cell has been improved by more than 15 dB with reference to the selectivity of the 1st order cell [Fig. 2(c)]. This fact implies that for frequencies below 0.4f_0, a dichroic mirror composed of 3rd order TEM cells will behave nearly like a perfect conducting sheet.

Figs. 8(a)-(b) show the S-parameters of the unit cell [Fig. 7(a)] calculated by CST and the equivalent circuit [Fig. 7(b)] for different angles of incidence (θ). The reflection coefficient for both TE [Fig. 8(a)] and TM [Fig. 8(b)] remains below -10 dB over 0.92~1.1f_0 (18% relative bandwidth) for incidence up to θ=50°. Fig. 8(c) depicts the phase difference between the TE and TM transmission coefficients. The phase imbalance gets values above 10° for incidence greater than 20°, which dictates a significant degradation with respect to the phase response of the 1st order TEM unit cell [Fig. 3(c)]. This is attributed to the higher axial length (d) of the 3rd order unit

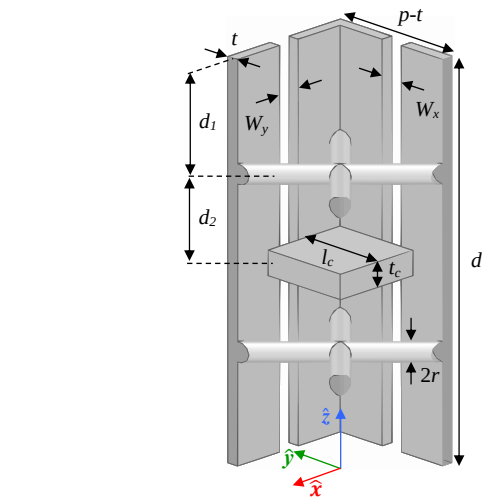

(a)

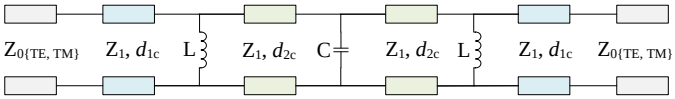

(b)

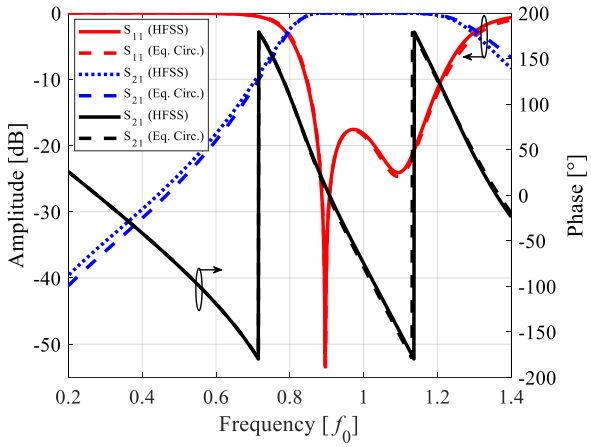

(c)

Fig. 7. The 3rd order TEM unit cell: (a) layout and geometrical parameters (p=0.265λ_0, d=0.672λ_0, t=0.021λ_0, r=0.017λ_0, w_x=w_y=0.042λ_0, l_c=0.16λ_0, t_c=0.042λ_0, d_1=0.189λ_0, d_2=0.147λ_0), (b) proposed equivalent circuit and (c) calculated S-parameters for an incident angle of {φ=0°, θ=0°}, for both TE and TM incidences (identical in this case) and with equivalent circuit values: Z_0≈376.73 Ω, Z_1=125 Ω, d_{1c}=0.193λ_0, d_{2c}=0.177λ_0, L=0.331 nH, C=13.7 fF.

cell with respect to the 1st order case. The values of the equivalent circuit's components are given in Table III.

III. Final Design Oriented to 3D-Printing

A. *Design Adaptations for 3D-Printing Compatibility*

This section describes the steps towards a co-design that complies with the AM rules. As known, during the 3D-printing process the structure that is built needs to be self-supported [44]. This means that overhanging metallic regions must be eliminated from the total body of the structure. This is typically achieved when the design does not present metallic inclinations greater than 45°.

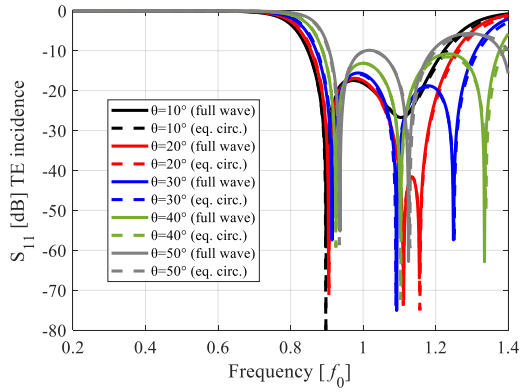

(a)

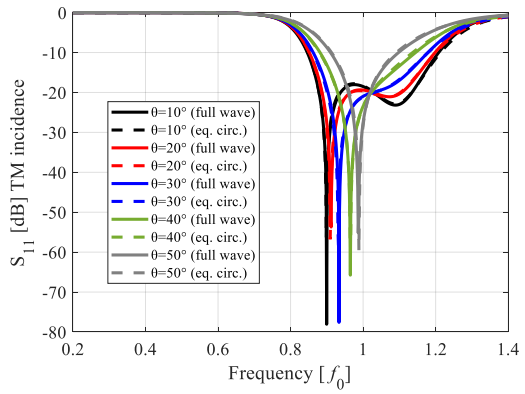

(b)

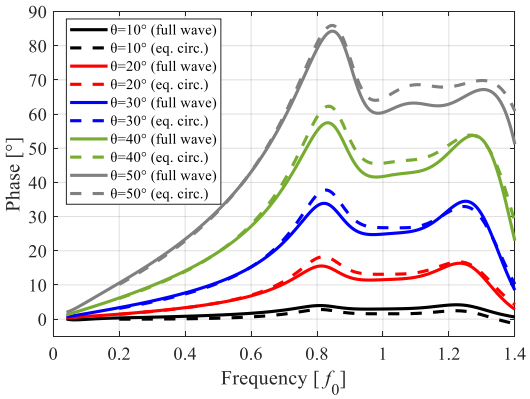

(c)

Fig. 8. Simulation results of the 3rd order TEM unit cell in Fig. 4(a): (a) reflection coefficient for TE incidence (E_y component), (b) reflection coefficient for TM incidence (E_x component) and (c) phase difference ($\Delta\varphi^{error}$) between the TE and TM transmission coefficients. The equivalent circuit's values [Fig. 4(b)] can be found in Table III [Z_1=125 Ω, $Z_{0,TE} = Z_0/\cos(\theta)$, $Z_{0,TM} = Z_0 \cdot \cos(\theta)$, $Z_0 \approx 376.73$ Ω].

TABLE III
EQUIVALENT CIRCUIT VALUES OF THE 3RD ORDER UNIT CELL [FIG. 7A)]

	d_{1c} [λ_0]	d_{2c} [λ_0]	L [nH]	C [fF]
θ=10°, TE	0.192	0.175	0.331	13.8
θ=10°, TM	0.193	0.177	0.331	13.8
θ=20°, TE	0.188	0.171	0.327	13.8
θ=20°, TM	0.194	0.177	0.332	13.8
θ=30°, TE	0.184	0.164	0.323	13.8
θ=30°, TM	0.196	0.177	0.334	13.8
θ=40°, TE	0.178	0.156	0.321	13.8
θ=40°, TM	0.199	0.177	0.333	13.8
θ=50°, TE	0.172	0.142	0.328	13.8
θ=50°, TM	0.203	0.177	0.332	13.8

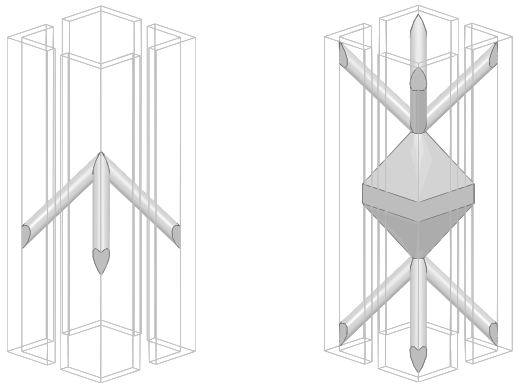

(a) (b)

Fig. 9. Geometrical modifications of the loads for a self-supported design adapted to the additive manufacturing technology: (a) modification of the inductive load (crossed bars) and (b) modification of the capacitive load (patch) connected to the two modified inductors.

Fig. 9(a) shows the first structural modification which relates to the inductive load. The four metallic arms of the inductive load that are connected to the junction of the cell's walls have been tilted by 45°. Fig. 9(b) shows the second modification for a design adapted to the 3D-printing technology and relates to the capacitive load and its connection to the lower and upper loads. Both faces of the metallic patch are flared to the connecting node of the four metallic arms of the inductive loads.

These structural modifications will have an impact on the unit cell's performance as the inductance and capacitance of the modified loads [Fig. 9(b)] will not have the same values in a circuit level as those of the cell in Fig. 7(a). However, as it will be later shown, the modified structures can always be represented as lumped inductive and capacitive loads with a different distribution along the cell's profile.

B. Optimized Design of the 3rd Order Blazed Unit Cell

The final optimized mechanical/RF co-design comprising the blazed concept, the adaptations of section II.A as well as some additional modifications in order to comply with the rules of 3D-printing technology is presented in Fig. 10.

As far as the three distinct parallel loads are concerned, the structure is similar to that of Fig. 9. The final geometrical modification considered in this optimized model relates to the flattening of the unit cell's lower and upper sections. On one hand, this was done in order to enhance the cells' walls thickness for the manufacturing process. Otherwise, with reference to Fig. 4(b), the lower and upper sections of the cell do not coincide with the metallic walls of adjacent cells and the thickness variable (t) would have to be of higher order degrading, therefore, the RF performance of the cell. On the other hand, a planar bottom section assures that the final dichroic mirror is self-supported as well.

These supplementary sections designed so that planar upper and lower parts are obtained, although are necessary mechanical modifications, they violate the blazed grating principle. This means that they induce some additional phase imbalance between the TE and TM transmission which denotes degradation of the XPD. Significant compensation of

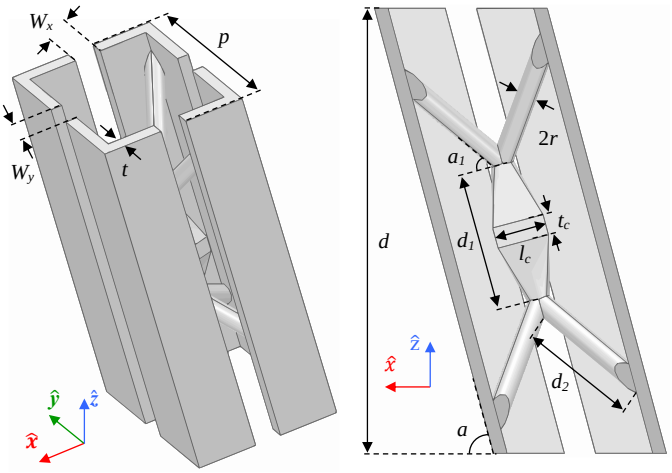

(a) (b)

Fig. 10. The optimized and AM-oriented 3rd order blazed TEM unit cell: layout and geometrical parameters (p=0.267λ_0, d=0.736λ_0, t=0.021λ_0, r=0.017λ_0, w_x=0.05λ_0, w_y=0.0425λ_0, l_c=0.083λ_0, t_c=0.033λ_0, d_1=0.226λ_0, d_2=0.232λ_0, a=15°, a_1=45°).

this transmission phase shift is achieved when considering slightly different widths of the lateral slits (i.e., $w_x \neq w_y$). A good trade-off between the blazed grating concept and the phase imbalance was the choice of a blaze angle equal to 15°. In the rest, the inductive and capacitive distribution of the three distinct loads connected in parallel along the cell's profile presents slight variations compared to the seminal design of Fig. 7(a). As a result, a fast tuning of the relative distance between the loads [variable d_1 from Fig. 10(b)] as well as the geometry of the capacitive element [variables t_c & l_c from Fig. 10(b)] was performed so as to minimize the reflection coefficients over the operating bandwidth, both TE and TM incidence as well as incident angles from 0° to 50°.

The simulated results of the final optimized 3rd order blazed unit cell are depicted in Fig. 11. For an incident angle of θ=30°, both TE and TM reflection coefficients remain below -10 dB over a fractional bandwidth of 27.5% (0.87~1.15f_0), while the transmission coefficient below 0.4f_0 (roll-off) is below -26 dB. This denotes that for frequencies below 0.4f_0, a dichroic mirror composed of such cells will behave nearly like a perfect conducting sheet.

The reflection coefficient for both TE [Fig. 11(a)] and TM [Fig. 11(c)] remains below -10 dB over 0.92~1.16f_0 (24% relative bandwidth) for incidence up to θ=50°. The phase imbalance gets values below 30° for incidence up to θ=50° (not shown for brevity). Fig. 11(e) depicts the XPD of the cell calculated according to eq. (5), where $E^t_{0,\,TE} = S_{21}^{\text{unit cell, TE}\rightarrow\text{TE}}$, $E^t_{0,\,TM} = S_{21}^{\text{unit cell, TM}\rightarrow\text{TM}}$ and $\varphi^t_{TE} = \text{phase}\left(S_{21}^{\text{unit cell, TE}\rightarrow\text{TE}}\right)$, $\varphi^t_{TM} = \text{phase}\left(S_{21}^{\text{unit cell, TM}\rightarrow\text{TM}}\right)$. The unit cell exhibits a cross-polar level (XPD) above 11 dB (AR<5 dB) for incidence up to θ=50° over 0.92~1.26f_0 (34% relative bandwidth) and above 16.5 dB (AR<2.6 dB) for incidence up to θ=40° over 0.9~1.19f_0 (29% relative bandwidth). The effective bandwidth for S_{11}<10 dB, XPD>16.5 dB and θ=0°~40° is 0.88~1.14f_0 (26% relative bandwidth). The equivalent circuit's [Fig. 7(b)] S-parameters show a perfect agreement with the ones from full-wave simulations. The values of the equivalent circuit's components are given in Table IV.

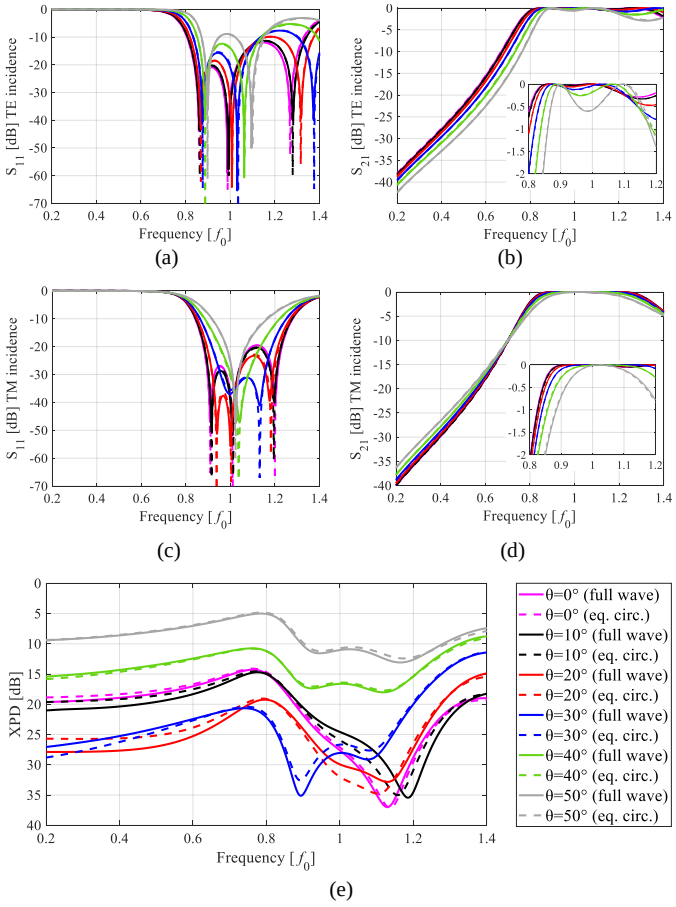

Fig. 11. Simulation results of the optimized and AM-oriented 3rd order blazed unit cell (Fig. 10): (a) reflection coefficient and (b) transmission coefficient for TE incidence (E_y component), (c) reflection coefficient and (d) transmission coefficient for TM incidence (E_x component) and (e) XPD. The equivalent circuit's values [Fig. 7(b)] are in Table IV [$Z_{0,TE} = Z_0/\cos(\theta)$, $Z_{0,TM} = Z_0 \cdot \cos(\theta)$, $Z_0 \approx 376.73\ \Omega$].

TABLE IV
EQUIVALENT CIRCUIT VALUES OF THE OPTIMIZED AND AM-ORIENTED 3RD ORDER BLAZED UNIT CELL (FIG. 10)

	Z_1 [Ω]	d_{1c} [λ_0]	d_{2c} [λ_0]	L [nH]	C [fF]
θ=0°, TE	122	0.187	0.1817	0.41	1.6
θ=0°, TM	127	0.19	0.1875	0.37	1.6
θ=10°, TE	120	0.186	0.18	0.4	1.8
θ=10°, TM	128	0.19	0.1875	0.37	1.6
θ=20°, TE	115	0.1825	0.1767	0.38	1.4
θ=20°, TM	134	0.19	0.1875	0.39	1.2
θ=30°, TE	105	0.1775	0.1708	0.34	1
θ=30°, TM	145	0.1917	0.1883	0.42	1
θ=40°, TE	94	0.1725	0.1633	0.3	0.8
θ=40°, TM	164	0.1925	0.1883	0.48	0.8
θ=50°, TE	77	0.1675	0.155	0.24	0.6
θ=50°, TM	195	0.1967	0.1892	0.57	0.6

IV. Prototyping and Experimental Results

A. Fabrication Strategy

The adaptations considered in sections III.A and III.B involved a rigorous mechanical/RF co-design process so that a structurally feasible and electromagnetically robust unit cell could be obtained. In this section, we introduce the fabrication strategy that was followed in order to facilitate a robust printing process.

This two-step strategy is illustrated in Fig. 12. After initially defining the minimum dimensions of the dichroic mirror for manufacturing and testing, we concluded that a mirror comprising an array of 19×19 blazed TEM unit cells (Fig. 10) is sufficient for the proof of the concept. Thus, the first step of the fabrication strategy relates to the design of a triangular ramp-like structure elongated below the initial blazed mirror's structure. This allows the printing of the cells in a vertical orientation, a fact that is very crucial in additive manufacturing as it minimizes the tolerances of the fabrication process as well as the surface roughness of periodic or waveguide structures [44]-[47]. Moreover, given that the cell's inductive loads (inclined metallic bars from Fig. 10) are already tilted by 45°, the blazed architecture of the cell induces an additional inclination equal to the blaze angle (15° in this case). As a result, if this fabrication strategy had not been followed, the cells' loads would have been 3D-printed with a total angle of 45°+15°=60°, forming therefore overhanging regions. This would bring high risk to the 3D-printing process and could hence be catastrophic in terms of RF performance.

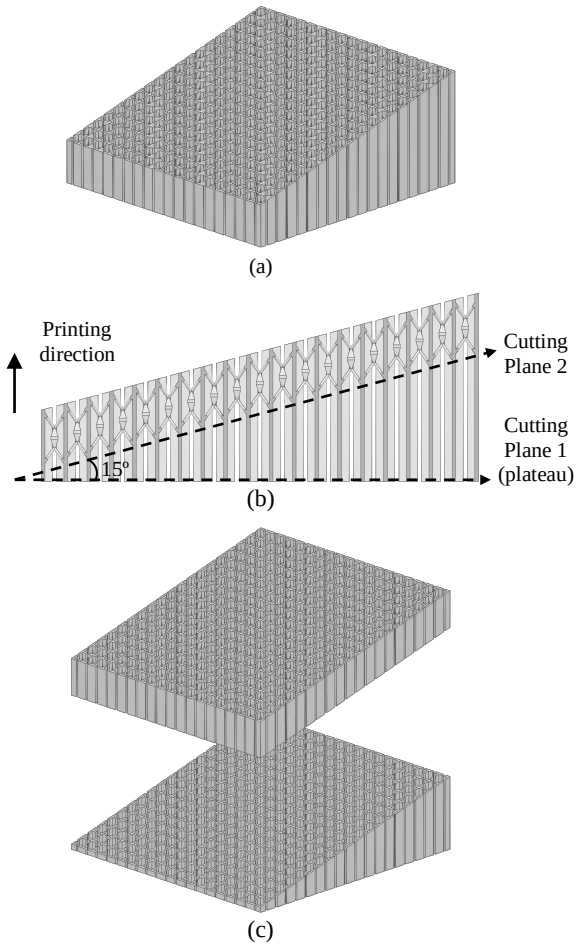

Fig. 12. Manufacturing strategy for the avoidance of overhangs by a CAD model of an array of 19×19 array blazed unit cells from Fig. 10: (a) perspective view of the model to be 3D-printed, (b) side-cut view of the structure to be 3D-printed and (c) illustration of the removal of the lower part with wire erosion (the upper part is the mirror to be characterized).

The last step of the fabrication strategy is depicted in Fig. 12(c), where the metallic ramp added below the dichroic mirror will finally be removed through wire erosion. In this stage, it is of high importance to first control the cutting angle (equal to the blaze angle, a) during the wire erosion process in order to assure a straight removal of the lower part. Last, it is equally important to control the starting point of the cutting process in order to minimise errors with respect to a precise removal (i.e., respecting the optimized cell's height).

B. Manufacturing and Experimental Results

With view to validate the concepts reported in this work, two dichroic mirrors comprising an array of 19×19 array blazed unit cells (Fig. 10) have been manufactured and tested. The central frequency of operation is 15 GHz (where λ_0 is defined).

Two mirrors [Fig. 13(a)] were 3D-printed simultaneously using aluminium powder (AlSi10Mg) by our industrial partner *3D-MetalPrint* [48]. The printing of two prototypes allows us to verify the repeatability of the printing and cutting process. The printer that was used is the DMP Flex 350 from 3D systems. The precision of the SLM process and hence the manufacturing tolerances are of the order of ±100 μm to ±150 μm. The two initial (as built) prototypes are depicted in Fig. 13(a) just after the 3D-prinitng process. Fig. 13(b) shows the top surface in zoom view for one of the mirrors. The two mirrors were later removed from the printing plateau with wire-erosion as printed (i.e., horizontally with reference to the plateau's surface) and were latter subjected to wire-erosion according to the strategy described in section IV.A and Fig. 12. One of the two final prototypes is shown in Fig. 13(c).

The experiments have been performed using the near-field multi-probe scanner for antenna pattern measurements of MVG StarLab chamber, whose operation range is 0.6 to 18 GHz [49]. The details of the device under test (DUT) and its positioning within the chamber are depicted in Fig. 13(d). For the measurements of the reflection coefficient [S_{11}], the 4-port VNA Rohde & Schwarz ZVA67 has been used.

The setup is similar to the one followed in [30]. The DUT consists of a linearly polarized horn with a size of 50×50×145 mm^3, that illuminates the dichroic mirror, which is tilted by 30° and positioned at a given distance from the aperture of the horn by a custom support. The horn's aperture diameter is around 50 mm corresponding to a broadside gain of around 17 dBi at 15 GHz. Such a design assures that the power level reaching the edges of the dichroic mirror is at least 10 dB lower than the level at its the centre (considering the spacing of 30 mm). This fact assures that most of the energy is captured by the dichroic mirror and a negligible radiation level

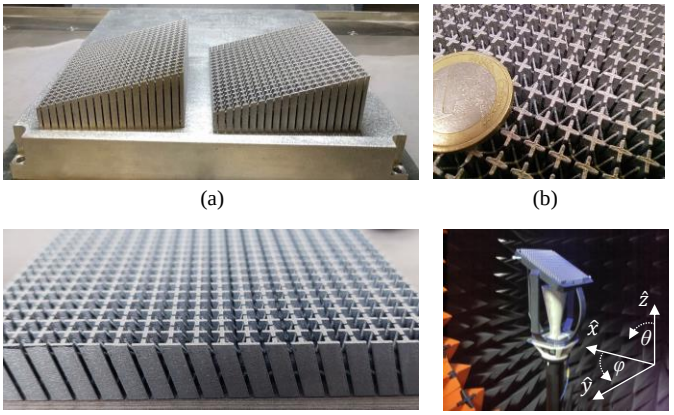

Fig. 13. Prototype of the dichroic mirror 3D-printed in aluminum SLM and measurement setup: (a) the two raw prototypes just after the 3D-printing, (b) zoom view of the top cells, (c) one prototype after the wire-cutting of the bottom part and (d) measurement setup in the StarLab.

will reach its edges or the support. Diffraction is thus avoided, as well as other possible sources of indirect radiation that mirror's influence on the horn's radiation patterns. The support has been modelled as a dielectric material with $\varepsilon_r = 3$ and $\tan\delta = 0.02$, values that emulate the photosensitive resin used to 3D-print the support. The size of the total measurement setup is 130×130×215 mm^3. Figure 13(d) shows also the coordinate system of the setup.

The measured results are presented in Figs. 14 to 18. Figures 14(a) and 14(b) show the simulated and measured reflection coefficients for TE and TM incidence, respectively. A good agreement between numerical and experimental results is observed. The input waveguide port of the horn antenna has $f_c \approx 8$ GHz. The horn antenna presents S_{11}<10 dB from 9.2 GHz, while the resonance occurring around 17 GHz corresponds to the excitation of the first higher order mode.

Figures 15(a) to 15(h) show the radiation patterns at two frequency points, 15 GHz and 9.25 GHz. The first frequency point (i.e., 15 GHz) is the centre of the bandwidth of interest (around 13.3-17 GHz i.e., 25% relative bandwidth), namely where the dichroic mirror presents its bandpass response. The second frequency point (i.e., 9.25 GHz) corresponds, on one hand, to the lowest frequency point where the horn antenna operates for S_{11}<10 dB, while on the other hand, to $0.6f_0$, where the rejection of the mirror [or the S_{21} response of the unit cell from Figs. 11(b) and 11(d)] is below -15 dB and therefore can be considered to emulate nearly a metallic sheet. A good agreement between simulations and measurements is observed. The increased measured cross-polar level with respect to simulations [e.g., in Figs. 15(a), 15(b), 15(e) and 15(f)] is attributed to the antenna alone. In other words, the cross-polar level of the antenna alone was measured (not shown for brevity) equivalent to the measurements of the system horn+mirror. This is attributed to mechanical tolerances of the horn antenna prototype. It is mentioned that the simulated cross-polar level of the unit cell (i.e., $S_{21}^{\text{unit cell, TE}\rightarrow\text{TM}}$ and $S_{21}^{\text{unit cell, TM}\rightarrow\text{TE}}$) is below -80 dB, so the mirror is not expected to bring additional cross-polar level in the total system.

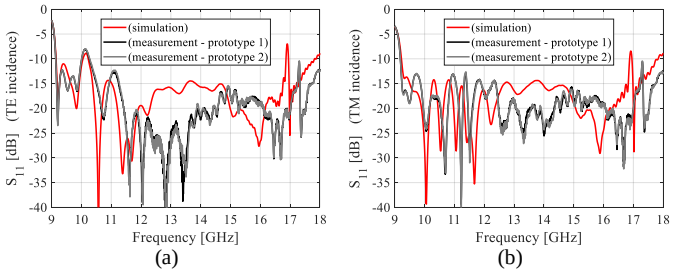

Fig. 14. Simulated and measured reflection coefficient of the system (dichroic mirror + horn) for: (a) TE and (b) TM incidence.

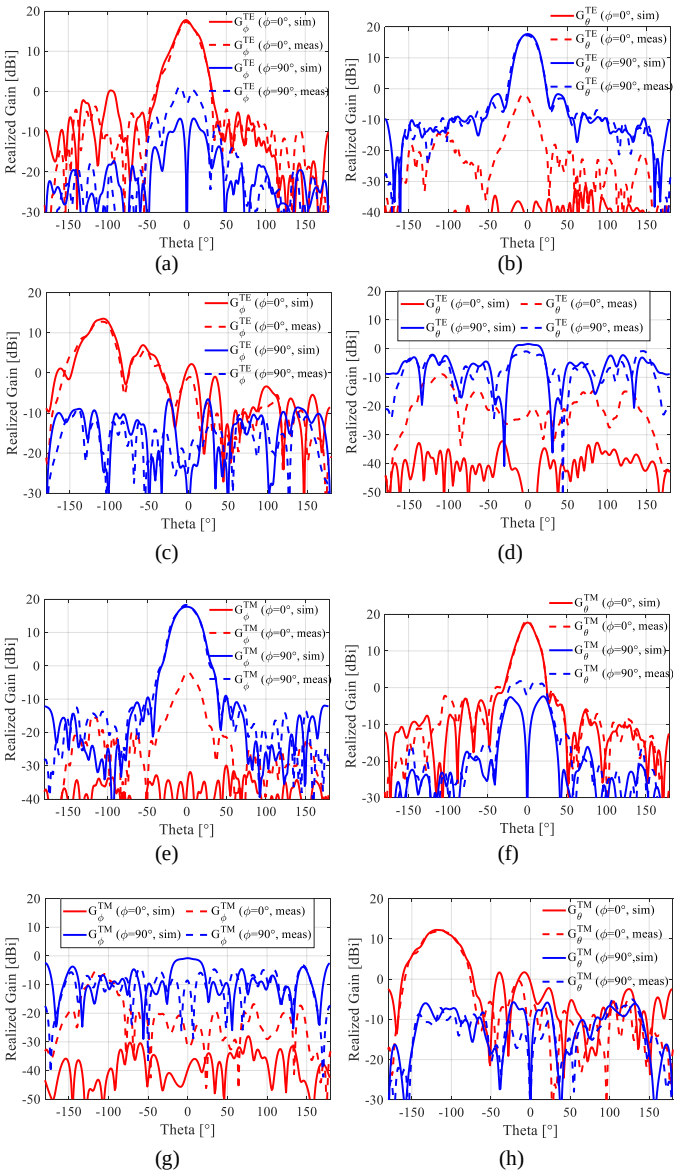

Fig. 15. Simulated and measured (prototype 1) radiation patterns of the system (dichroic mirror + horn): (a) G_φ TE incidence at 15 GHz, (b) G_θ TE incidence at 15 GHz, (c) G_φ TE incidence at 9.25 GHz, (d) G_θ TE incidence at 9.25 GHz, (e) G_φ TM incidence at 15 GHz, (f) G_θ TM incidence at 15 GHz, (g) G_φ TM incidence at 9.25 GHz and (h) G_θ TM incidence at 9.25 GHz.

Another point relates to the specular component of the radiation patterns for the system horn+mirror. Figs. 15(c) and 15(h) show that this is -108° and -116° for TE and TM incidence, respectively, while the precise specular direction is

normally -120° (with reference to the broadside as: -90°-30°) as a function of the mirror's tilt angle of 30°. This is attributed to the fact that the mirror is placed in the near-field region of the antenna's phase centre and therefore the plane wave approximation (as in the case of the unit cell analysis) is no longer valid leading to this phenomenon of smaller than the nominal specular angles. We have also performed measurements of a metallic sheet at the place of the dichroic mirror which have verified the above point of smaller than the nominal specular angles.

In order to monitor the performance of the mirror in a wide frequency range, we continue to Figs. 16 to 18. First, Figs. 16(a) and 16(b) depict the simulated and measured maximum realized gain in all directions across the frequency of the measurement setup for TE and TM incidence, respectively. Owing to the frequency selective nature of the DUT, it is expected that the in the upper band (i.e., above 13 GHz) the main lobe of the system's gain is on broadside direction, while in the lower band (i.e., roughly below 11 GHz) the gain in the specular direction should become higher than the broadside one. Although the gain curves between simulations and measurements show a good agreement, a drop of the measured gain values below 13.5 GHz is observed.

As a result, we performed further analysis of this data, separating the two directions of the realized gain, meaning the broadside and the specular ones. First, Figs. 17(a) and 17(b) show the simulated (solid lines) and measured (dashed lines) broadside (red lines) and specular (blue lines) maximum realized gain of the configuration used as a measurement setup in Fig. 13(d). In the same graphs, the simulated and measured broadside realized gain of the horn alone are also plotted. Several interesting observations have been derived by these two graphs. First, the proof-of-concept of this work is clearly clarified by the illustrated filtering response of the DUT across a wide frequency bandwidth. This is clearly depicted in both graphs given the fact that the simulated specular realized gain below 12 GHz becomes more dominant than the broadside one denoting the reflective behaviour of the DUT. Second, in the higher frequencies the dichroic mirror becomes transparent for the radiation of the horn denoting the transmissive behaviour of the DUT. The simulated and measured peak realized gain values in the higher band between the system horn/mirror and the horn alone are in good agreement.

Third, a frequency shift of around 1.9 GHz and 1.6 GHz for TE and TM incidence, respectively, is observed between simulations and measurements. This systematic for both TE and TM incidences frequency shift is mainly attributed to manufacturing deflections of the SLM process as well as the wire-cutting process as a post-fabrication step. Other root causes for these discrepancies relate to the complexity of the system used as a DUT, inaccuracies in simulations and measurements, mechanical tolerances and structural divergences of the prototyped horn antenna, positioning non-idealities during measurements and potentially other systematic inaccuracies of StarLab's anechoic chamber.

Although the precise determination of the global root causes is a rather complicated process considering the complexity of

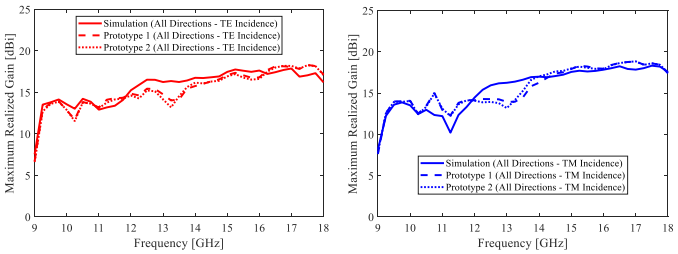

(a) (b)

Fig. 16. Simulated and measured maximum realized gain in all directions across the frequency of the measurement setup: (a) TE incidence and (b) TM incidence.

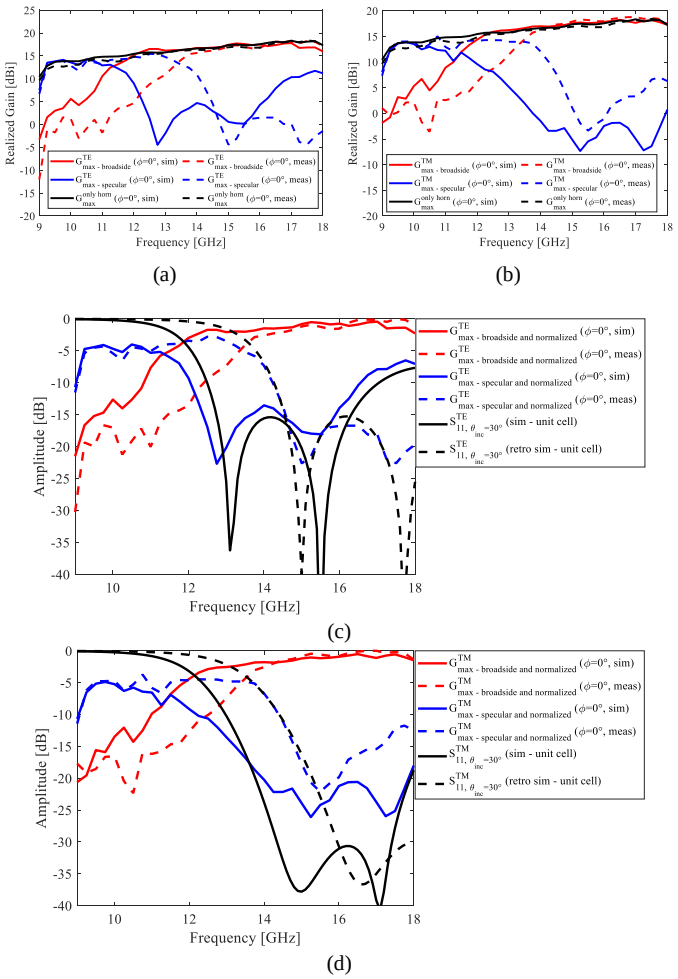

(a) (b) (c) (d)

Fig. 17. Simulated and measured maximum realized gain in broadside and specular directions of the measurement setup and realized gain in broadside for the horn alone across the frequency: (a) TE incidence, (b) TM incidence, (c) normalized gain and simulated S_{11} of the unit cell with nominal and retro-simulated values for TE incidence and (d) normalized gain and simulated S_{11} of the unit cell with nominal and retro-simulated values for TM incidence.

the different parts of the measurement configuration and the lack of tomographic analysis, we have further proceeded to a representative quantification of the manufacturing errors. Figs. 17(c) and 17(d) depict the normalized gain (both in broadside and specular directions) and simulated S_{11} of the unit cell with nominal (solid black line) and retro-simulated (dashed black lines) values for TE and TM incidence, respectively. The retro-simulations refer to the tolerance analysis of the unit cell with view to correlate the measurement declinations with

respect to the simulated realized gain values. The retro-simulated response of the unit cell's reflection coefficient for TE and TM incidence relate to geometrical modifications which correspond to a factor of 0.9 (i.e., smaller design values of an order of 10%). Although the sensitivity impact on the unit cell's S-parameters and the geometrical differentiation is not straightforward for all design variables, the above retro-simulation factor corresponds to structural alternations ranging from 40 μm (e.g. for the variables r, t, W_x, W_y) up to 400 μm (e.g. for the variables d, d_1 and d_2). Most of these structural differentiations are estimated to fall into the manufacturing tolerances of the 3D-printing process (i.e. around 150 μm). Further correlation studies as well as sensitivity and tomographic analyses are expected to bring significant information to the precise monitoring of the root causes for such misalignments between numerical calculations and experimental results. This would be the principal part of a project towards the industrialization of this concept and technology readiness level (TRL) maturation of a future product where high repeatability levels in manufacturing and series production are targeted.

Fig. 18 shows the simulated and measured broadside phase difference of the co-polar linearly polarized patterns for the cut φ=0° between TE (i.e., G_φ) and TM (i.e., G_θ) incidence. In the same graph, the phase difference ($\Delta\varphi^{error}$) between the TE and TM transmission coefficients (S_{21}) for an incidence angle θ=30° of the optimized and AM-oriented 3rd order blazed TEM unit cell (Fig. 10) is also plotted. Since the specular angle in measurements and simulations as well as for different frequency points is not stable, we plot and compare the phase difference where the dichroic mirror operates in transmission (i.e., above 13.5 GHz). A good agreement between simulated and measured results is observed. This fact denotes that the dichroic mirror induces low phase difference between TE and TM incidence, which, in turn dictates high XPD levels and hence CP-purity. The slight discrepancies between numerical and experimental results in Fig. 18 (red lines), are attributed to manufacturing tolerances. It is noted that according to our retro-simulations, the phase difference between TE and TM incidence [i.e., $\Delta\varphi^{error}$ from eq. (4)] presents very low differentiations with respect to the tolerance analysis.

In order to capture the phase response of the mirror, we proceed to the reconstruction of the circular-polarization (CP) radiation patterns. We first write the two orthogonal components of the spherical coordinates realized gain radiation patterns, G_θ and G_φ, as:

$$G_\theta=\frac{1}{\sqrt{2}}\left(G_\theta^{TE}+jG_\theta^{TM}\right) \quad \text{where } G_\theta^{TE}=\left|G_\theta^{TE}\right|e^{-j\arg\left(G_\theta^{TE}\right)} \ \& \ G_\theta^{TM}=\left|G_\theta^{TM}\right|e^{-j\arg\left(G_\theta^{TM}\right)} \tag{9a}$$

$$G_\varphi=\frac{1}{\sqrt{2}}\left(G_\varphi^{TE}+jG_\varphi^{TM}\right) \quad \text{where } G_\varphi^{TE}=\left|G_\varphi^{TE}\right|e^{-j\arg\left(G_\varphi^{TE}\right)} \ \& \ G_\varphi^{TM}=\left|G_\varphi^{TM}\right|e^{-j\arg\left(G_\varphi^{TM}\right)} \tag{9b}$$

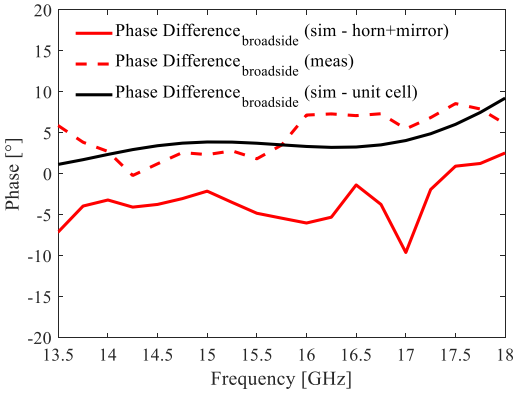

Fig. 18. Simulated and measured broadside phase difference of the co-polar patterns for the cut φ=0° between TE (i.e., G_φ) and TM (i.e., G_θ) incidence.

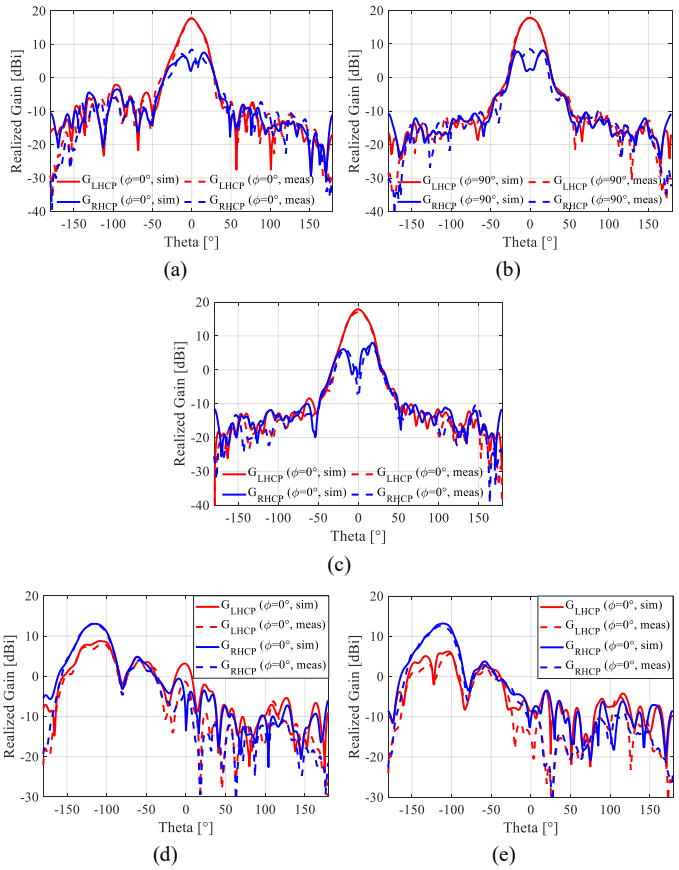

Fig. 19. Simulated and measured CP realized gain radiation patterns: (a) the system horn+mirror [measurement setup in Fig. 13(d)] at 15GHz and φ=0°, (b) the system horn+mirror at 15GHz and φ=90°, (c) the horn alone at 15 GHz and φ=0° (at φ=90° are the same patterns), (d) the system horn+mirror at 9.5GHz and φ=0° and (e) the system horn+metallic sheet at 9.5GHz and φ=0°.

As can be seen, the components G_θ^{TE}, G_θ^{TM}, G_φ^{TE}, and G_φ^{TM} are in polar form, hence their phase is included herein. The left-hand circularly polarized (LHCP) and right-hand circularly polarized (RHCP) patterns, are calculated as:

$$G_{LHCP}=\frac{1}{\sqrt{2}}\left(G_\theta+jG_\varphi\right) \tag{10a}$$

$$G_{RHCP}=\frac{1}{\sqrt{2}}\left(G_\theta-jG_\varphi\right) \tag{10b}$$

Figures 19(a) and 19(b) show the simulated and measured CP realized gain radiation patterns of the system horn+mirror [measurement setup in Fig. 13(d)] at 15GHz at φ=0° and φ=90° cut, respectively. Figure 19(c) shows the equivalent simulated and measured patterns of the horn antenna alone (without the dichroic screen). First, a very good agreement between measurements and simulations is observed. Second, the patterns of Figs. 19(a) and 19(b) which correspond to the reconstruction of the CP fields from the TE and TM incidences, agree very well to the patterns of Fig. 16(c), denoting that the mirror is transparent in terms of transmission amplitude and induces low phase shift [$\Delta\varphi^{\text{error}}$ from eq. (4)].

Similarly, Figs. 19(d) and 19(e) show the CP realized gain radiation patterns of the system horn+mirror [measurement setup in Fig. 13(d)] at 9.5GHz (φ=0° cut) and those of the system horn+metallic sheet (φ=0° cut), respectively. In other words, we compare here the simulated and measured specular radiation occurring when placing the horn below the mirror (i.e., at 9.5GHz the rejection level is above 15 dB) and below a totally opaque metallic screen (an aluminum sheet) at the same frequency. A close agreement between numerical and experimental results as well as specular radiation including the horn and a perfect reflecting screen is also observed here.

The last experimental results of the dichroic mirror in terms of radiation patterns and maximum realized gain are presented in Figs. 20 and 21, respectively. Fig. 20 depicts the radiation patterns of the lower and higher frequencies of the mirror's operating bandwidth. Figs. 20(a) and 20(b) show the simulated and measured CP realized gain radiation patterns of the system (dichroic mirror + horn) at 13.25GHz and in two cut planes (i.e., φ=0° and φ=90°, respectively), while Figs. 20(c) and 20(d) show the simulated and measured CP realized gain radiation patterns at 17.25GHz and for the same cut planes. In all figures, we have also plotted the simulated radiation patterns at lower frequencies in order to correlate the simulated and measured data as a further analysis and verification of the frequency shift that was observed above in the peak realized gain values. Thus, Figs. 20(a) and 20(b) show that the measured radiation patterns at 13.25 GHz correlate with a good agreement (both in peak gain and in off-broadside radiation) with the simulated ones at 11.25 GHz denoting a frequency shift of around 2 GHz. Similarly, Figs. 20(c) and 20(d) show that the measured radiation patterns at 17.25 GHz of the setup correlate with a good agreement (both in peak gain and in off-broadside radiation) with the simulated ones at 15.75 GHz denoting a frequency shift of around 1.5 GHz. As a result, an average frequency shift of 1.75 GHz is captured by these correlations which is in line with the frequency shift shown in the peak realized gain of Fig. 17 (i.e., 1.9 GHz and 1.6 GHz for TE and TM incidence, respectively).

Figs. 21(a) and 21(b) show the simulated and measured broadside and peak specular LHCP/RHCP realized gain of the measurement setup, respectively. As expected, a gain drop in the measured results of Fig. 21(a) and a gain increase in the measured results of Fig. 21(b) below 14 GHz is observed which is related to the frequency shift of around 1.75 GHz between simulations and measurements. The reasons for these discrepancies have been discussed above and relate principally to manufacturing tolerances of the prototypes (both in the 3D-printing process for the horn and the mirror as well as the

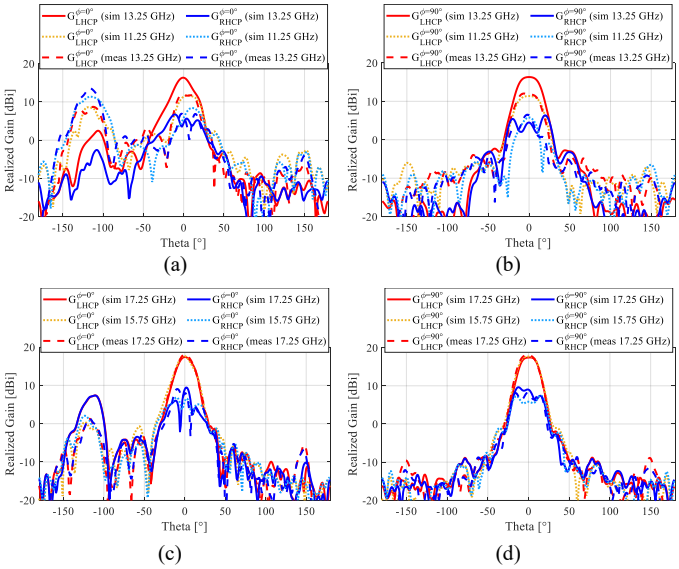

Fig. 20. Simulated and measured CP realized gain radiation patterns of the system (dichroic mirror + horn) at 13.25GHz and 17.25 GHz (with the simulated one at lower frequencies for correlation of the simulated and measured data): (a) at 13.25 GHz and φ=0° (together with the simulated at 11.25 GHz), (b) at 13.25 GHz and φ=90° (together with the simulated at 11.25 GHz), (c) at 17.25 GHz and φ=0° (together with the simulated at 15.75 GHz) and (d) at 17.25 GHz and φ=90° (together with the simulated at 15.75 GHz).

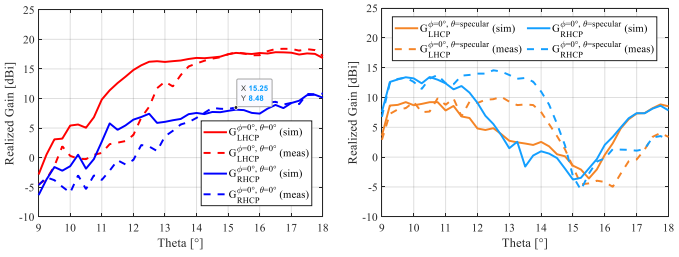

Fig. 21. Simulated and measured CP realized gain vs frequency of the setup in Fig. 13(d) (system horn+mirror): (a) broadside and (b) specular.

wire-cutting process of the mirror). Apart from these discrepancies, the results show a good agreement between measurements and simulations in terms of the filtering response of the mirror.

All simulations have been performed using an effective conductivity value of 10 MSiemens/meter in order to take into account the additional losses induced to the unit cell due to the 3D-printing process and the associated surface roughness of this manufacturing technique. Although the measurement setup employed in this work is not suitable for precisely characterizing the dichroic mirror's ohmic losses, we consider this assigned effective conductivity value as an accurate approximation of the structure's additional losses related to the surface roughness of the 3D-printing process according to our prior experience [33], [44]-[47] and the literature [50]-[56]. In particular, in Ku-band and for vertical printing of periodic structures or waveguide components in aluminum alloy AlSi10Mg produced by SLM, which also employ parts printed in 45°, the surface roughness is of the order of 5–20 μm Ra, inducing an equivalent electrical conductivity of the order of 5-15 MSiemens/meter. According to simulations, for

TABLE IV
COMPARISON OF STATE-OF-THE-ART FULL-METAL FSS

Ref. →	[15]	[23] - D1	[23] - D6	[32]	This work
Operating Freq. [GHz]	7.1 - 8.5	22.55 - 27	22.55 - 23.15 25.5 - 27	9.58 -11.86	13.2 - 17.1
BW [%]	18	18	2.5 & 6	21.2	25
RL [dB]	10	10	10	N/A	10
XPD [dB]	20	20	24	N/A	16.5
IL [dB]	0.5	>1	0.5	3	0.5
Angular Range (°)	25~35	25~35	25~35	0~45	0~40
Thickness (λ_0)	0.75	0.76	1.42	0.65	0.73
Periodicity (λ_0)	0.69	0.65	0.66	0.43	0.27
Manuf. Process	Milling	Milling	Wire erosion	Laser cutting	SLM

these levels of effective conductivity, the ohmic losses of the unit cell vary between 0.05 and 0.1 dB.

Table IV shows the state-of-the-art full-metal FSS related to this work. Current practice for Deep Space applications relies on the full-metal dichroic mirror solution which employs the concept of the conducting screen perforated periodically with apertures [15], [23]. This solution employs cells with a periodicity above half of a wavelength and present typically limited angular stability in terms of return losses and XPD. Last, in [32] we can find a fully metallic FSS with a bandpass filtering function, operating over a relative bandwidth of 21.2% and over a wide angular range for a 3-dB insertion loss though. Nevertheless, this solution is not a candidate for dichroic mirrors as the XPD analysis was out of the scope of this work. As a result, Table IV shows that the proposed solution based on the metal-only PPW-cell, the high level of miniaturization and the blazing architecture can overcome the limitations posed by the state-of-the-art in terms of operating frequency bandwidth, angular range and RF performance.

V. CONCLUSION

This paper presents a dichroic mirror architecture based on a blazed grating topology and exploiting the PPW unit cell. The high-pass filtering response (low-band selectivity) is achieved by cascaded inductive and capacitive loads designed according to the 3D-printing rules. High miniaturization has been achieved (subwavelength periodicity of the order of $0.27\lambda_0$) through the TEM-like behavior (no cut-off) of the cell leading to high angular stability. The blazed topology assures an efficient performance in terms of XPD for a tilting angle illumination of 30°. The 3rd order filtering synthesis provides the required low-band roll-off. The equivalent circuit analysis agrees almost perfectly to full-wave simulations owing to the subwavelength periodicity of the unit cell. These, for both TE and TM incidence, show an S_{11}< -10 dB as well as an XPD>16.5 dB (AR<2.6 dB) over a relative bandwidth of 25% and an angular range up to θ=40°, when CP-incidence is considered.

After introducing the related fabrication strategy for robust additive manufacturing, two prototypes have been manufactured through SLM and tested through a custom measurement setup. Taking into consideration a frequency shift of around 1.7 GHz that was monitored between the measurement and simulation results, a good agreement both in terms of S-parameters and radiation patterns has been demonstrated, verifying the concept of this work. The performed sensitivity analysis showed good correlation between retro-simulations and measurements dictating the principal root cause of these discrepancies which are the manufacturing tolerances of the fabrication and wire-cutting process.

Future steps of this work relate to an entirely industrialization framework of the proposed concept. Detailed definition of geometrical divergences occurring from the fabrication process, alternative and more adapted fabrication techniques, tomographic analyses for the precise determination of the root causes as well as studies on the minimization of those by better controlling and optimizing the 3D-printing and wire-cutting process are candidate elements and activities to be included in this framework. The significance of such an industrial project relates, on one hand, to the upgrade of the concept's TRL and, on the other hand, to challenges which will occur when scaling of the dichroic mirror to commercial frequency bands will be needed to be realized. These challenges relate principally to volumetric issues and manufacturing techniques when scaling down to lower frequencies as well as fabrication precision and resolution when scaling up to higher frequencies. It is last noted that metal-only 3D-printing (e.g., SLM) is a highly evolving manufacturing technique and is well adapted to the development of periodic and grid-like structures. Given this dramatic evolution and rapid progress of the additive manufacturing domain over the last two decades, significant improvement in terms of quality (i.e., resolution), speed, process automation, technological maturity and industrial readiness is therefore expected.

ACKNOWLEDGEMENTS

The authors want to thank Pr. Renaud Loison, professor of INSA Rennes, Dr. Andrea Guarriello, post-doctoral fellow of INSA Rennes and Dr. Juan-Antonio Duran-Venegas, engineer of Thales Alenia Space, for their fruitful discussions and advice. They want also to thank the technician Jérôme Sol of INSA Rennes for his help with the measurements. Last, the authors want last to thank Maxime Hugues, Director of 3D-MetalPrint, for his contribution to the prototyping of the two dichroic mirrors.

REFERENCES

[1] B. A. Munk, *Frequency Selective Surfaces: Theory and Design*. New York: Wiley-Interscience, 2011.
[2] D. M. Pozar, *Microwave Engineering*, 4th ed. New York, NY, USA: Wiley, 2012.
[3] M. Born and E. Wolf, *Principles of Optics: Electromagnetic Theory of Propagation, Interference and Diffraction of Light*, 7th ed. Cambridge, U.K.: Cambridge Univ. Press, 1999.
[4] A. Patri, S. Kéna-Cohen and C. Caloz, "Large-angle broadband and multifunctional directive waveguide scatterer gratings," *ACS Photon.*, vol. 6, no. 12, 6, pp. 3298−3305, Dec. 2019.
[5] E. Treacy, "Optical pulse compression with diffraction gratings," *IEEE J. Quantum Electron.*, vol. 5, no. 9, pp. 454–458, Sep. 1969.
[6] S. L. Dobson, P. -C. Sun and Y. Fainman, "Diffractive lenses for chromatic confocal imaging," *Appl. Opt.*, vol. 36, no. 20, pp. 4744−4748, Jul. 1997.
[7] T. Itoh and R. Mittra, "An Analytical Study of the Echelette Grating with Application to Open Resonators," *IEEE Trans. Microw. Theory and Techn.*, vol. 17, no. 6, pp. 319-327, June 1969.

[8] C. Antoine, X. Li, J.-S. Wang and O. Solgaard, "Reconfigurable optical wavelength multiplexer using a MEMS tunable blazed grating," *J. Lightw. Technol.*, vol. 25, no. 10, pp. 3001–3007, Oct. 2007

[9] X. Li, C. Antoine, D. S. Lee, J. S. Wang and O. Solgaard, "Tunable blazed gratings," *J. Microelectromech. Syst.*, vol. 15, pp. 597–604, June 2006.

[10] C. Molero, R. Rodriguez-Berral, F. Mesa and F. Medina, "Analytical circuit model for 1-D periodic T–shaped corrugated surfaces," *IEEE Trans. Antennas Propag.*, vol. 62, no. 2, pp. 794–803, Feb. 2014.

[11] X. Li, M. Memarian, K. Dhwaj and T. Itoh, "Blazed metasurface grating: The planar equivalent of a sawtooth grating," *IEEE MTTS Int. Microw. Symp. Dig.*, San Francisco, CA, USA, May 2016, pp. 22–27.

[12] M. Memarian, X. Li, Y. Morimoto and T. Itoh, "Wide-band/angle blazed surfaces using multiple coupled blazing resonances," *Sci. Rep.*, vol. 7, Feb. 2017, Art. no. 42286.

[13] W. A. Imbriale, *Large antennas of the Deep Space Network.* New York: Wiley-Interscience, 2003.

[14] E. Vassallo *et al.*, "The European Space Agency's Deep-Space Antennas," *Proc. IEEE*, vol. 95, no. 11, pp. 2111-2131, Nov. 2007.

[15] P. Besso, M. Bozzi, L. Perregrini, L. S. Drioli and W. Nickerson, "Deep-space antenna for Rosetta mission: design and testing of the S/X band dichroic mirror," *IEEE Trans. Antennas Propag.*, vol. 51, no. 3, pp. 388-394, Mar. 2003.

[16] M. Pasian, M. Bozzi and L. Perregrini, "Accurate Modeling of Dichroic Mirrors in Beam-Waveguide Antennas," *IEEE Trans. Antennas Propag.*, vol. 61, no. 4, pp. 1931-1938, Apr. 2013.

[17] J. C. Chen, "Computation of reflected and transmitted horn radiation pattern for a dichroic plate," JPL, Pasadena, CA, TDA Progress Rep. 42-119, 1994. [Online]. Available: https://ntrs.nasa.gov/api/citations/19950010878/downloads/19950010878.pdf

[18] M. Pasian, M. Formaggi, M. Bozzi, F. Carli, L. Perregrini, G. Philippou and G. Dauron, "Multiphysics Design and Experimental Verification of a Quad-Band Dichroic Mirror for Deep Space Ground Stations," *IET Microw., Antennas Propag.*, Vol. 7, No. 6, pp. 391–398, Apr. 2013.

[19] P. Vogel and L. Genzel, "Transmission and reflection of metallic mesh in the far infrared", *Infrared Phys.*, vol. 4, no. 4, pp. 257-262, Dec. 1964.

[20] C.-C. Chen, "Transmission through a Conducting Screen Perforated Periodically with Apertures," *IEEE Trans. Microw. Theory Techn.*, vol. 18, no. 9, pp. 627-632, Sep. 1970.

[21] C.-C. Chen, "Transmission of Microwave Through Perforated Flat Plates of Finite Thickness," *IEEE Trans. Microw. Theory Techn.*, vol. 21, no. 1, pp. 1-6, Jan. 1973.

[22] L. W. Epp, P. H. Stanton, R. E. Jorgenson and R. Mittra, "Experimental verification of an integral equation solution for a thin-walled dichroic plate with cross-shaped holes," *IEEE Trans. Antennas Propag.*, vol. 42, no. 6, pp. 878-882, June 1994.

[23] M. Marchetti, F. Pelorossi, F. Concaro, L. Perregrini and M. Pasian, "Comparative Study on the Design of Dichroic Mirrors for the Upgrade to the K-band uplink channel for the ESA Deep Space Antennas", *Proc. 15th Eur. Conf. Antennas Propag. (EuCAP'21),* pp. 1-5, Mar. 2021.

[24] A. K. Rashid, B. Li and Z. Shen, "An overview of three-dimensional frequency-selective structures," *IEEE Antennas Propag. Mag.*, vol. 56, no. 3, pp. 43-67, June 2014.

[25] D. Ferreira, I. Cuiñas, R. F. S. Caldeirinha and T. R. Fernandes, "3-D Mechanically Tunable Square Slot FSS," *IEEE Trans. Antennas Propag.*, vol. 65, no. 1, pp. 242-250, Jan. 2017.

[26] X. -J. Huang, C. Yang, Z. -H. Lu and P. -G. Liu, "A Novel Frequency Selective Structure With Quasi-Elliptic Bandpass Response," *IEEE Antennas Wireless Propag. Lett.*, vol. 11, pp. 1497-1500, 2012.

[27] R. Sivasamy and M. Kanagasabai, "Novel Reconfigurable 3-D Frequency Selective Surface," *IEEE Trans. Compon., Packag., Manuf. Technol.*, vol. 7, no. 10, pp. 1678-1682, Oct. 2017.

[28] D. Z. Zhu, M. D. Gregory, P. L. Werner and D. H. Werner, "Fabrication and Characterization of Multiband Polarization Independent 3-D-Printed Frequency Selective Structures With UltraWide Fields of View," *IEEE Trans. Antennas Propag.*, vol. 66, no. 11, pp. 6096-6105, Nov. 2018.

[29] C. Molero and M. García-Vigueras, "Circuit Modeling of 3-D Cells to Design Versatile Full-Metal Polarizers," *IEEE Trans. Microw. Theory Techn.*, vol. 67, no. 4, pp. 1357-1369, Apr. 2019.

[30] C. Molero Jimenez, E. Menargues and M. García-Vigueras, "All-Metal 3-D Frequency-Selective Surface With Versatile Dual-Band Polarization Conversion," *IEEE Trans. Antennas Propag.*, vol. 68, no. 7, pp. 5431-5441, Jul. 2020.

[31] J. Lundgren, O. Zetterstrom, F. Mesa, N. J. G. Fonseca and O. Quevedo-Teruel, "Fully Metallic Dual-Band Linear-to-Circular Polarizer for K/Ka-band," *Antennas Wireless Propag. Lett.*, vol. 20, no. 11, pp. 2191-2195, Nov. 2021.

[32] A. Lalbakhsh, M. U. Afzal, K. P. Esselle and S. L. Smith, "All-Metal Wideband Frequency-Selective Surface Bandpass Filter for TE and TM Polarizations," *IEEE Trans. Antennas Propag.*, vol. 70, no. 4, pp. 2790-2800, Apr. 2022.

[33] C. Molero, H. Legay, T. Pierré and M. García-Vigueras, "Broadband 3D-Printed Polarizer based on Metallic Transverse Electro-Magnetic Unit-Cells," *IEEE Trans. Antennas Propag.*, vol. 70, no. 6, pp. 4632-4644, June 2022.

[34] R. Sorrentino and O. A. Peverini, "Additive manufacturing: a key enabling technology for next-generation microwave and millimeter-wave systems [point of view]," *Proc. IEEE*, vol. 104, no. 7, pp. 1362-1366, Jul. 2016.

[35] C. Stoumpos, M. García-Vigueras, J. -A. Duran-Venegas and T. Pierré, "Additively Manufactured High Power Microwave Components in Aluminum SLM," *Proc. IEEE ICOPS*, pp. 1-1, Sep. 2021.

[36] K. Sarabandi and N. Behdad, "A Frequency Selective Surface With Miniaturized Elements," *IEEE Trans. Antennas Propag.*, vol. 55, no. 5, pp. 1239-1245, May 2007.

[37] N. Behdad, M. Al-Joumayly and M. Salehi, "A Low-Profile Third-Order Bandpass Frequency Selective Surface," *IEEE Trans. Antennas Propag.*, vol. 57, no. 2, pp. 460-466, Feb. 2009.

[38] M. Yan *et al.*, "A Miniaturized Dual-Band FSS With Second-Order Response and Large Band Separation," *Antennas Wireless Propag. Lett.*, vol. 14, pp. 1602-1605, Mar. 2015.

[39] S. M. A. Momeni Hasan Abadi and N. Behdad, "Wideband Linear-to-Circular Polarization Converters Based on Miniaturized-Element Frequency Selective Surfaces," *IEEE Trans. Antennas Propag.*, vol. 64, no. 2, pp. 525-534, Feb. 2016.

[40] B. Ashvanth, B. Partibane and M. G. N. Alsath, "An Ultraminiaturized Frequency Selective Surface With Angular and Polarization Stability," *Antennas Wireless Propag. Lett.*, vol. 21, no. 1, pp. 114-118, Jan. 2022.

[41] S. Dey, S. Dey and S. K. Koul, "Second-Order, Single-Band and Dual-Band Bandstop Frequency Selective Surfaces at Millimeter Wave Regime," *IEEE Trans. Antennas Propag*, vol. 70, no. 8, pp. 7282-7287, Aug. 2022

[42] M. A. Al-Joumayly and N. Behdad, "A Generalized Method for Synthesizing Low-Profile, Band-Pass Frequency Selective Surfaces With Non-Resonant Constituting Elements," *IEEE Trans. Antennas Propag.*, vol. 58, no. 12, pp. 4033-4041, Dec. 2010.

[43] D. Blanco and R. Sauleau, "Broadband and Broad-Angle Multilayer Polarizer Based on Hybrid Optimization Algorithm for Low-Cost Ka-Band Applications," *IEEE Trans. Antennas Propag.*, vol. 66, no. 4, pp. 1874-1881, Apr. 2018.

[44] M. García-Vigueras, L. Polo-Lopez, C. Stoumpos, A. Dorlé, C. Molero and R. Gillard, "Metal 3D-Printing of Waveguide Components and Antennas: Guidelines and New Perspectives", in Hybrid Planar - 3D Waveguiding Technologies [Working Title]. London, United Kingdom: IntechOpen, 2022.

[45] C. Stoumpos, J. -P. Fraysse, G. Goussetis, R. Sauleau and H. Legay, "Quad-Furcated Profiled Horn: The Next Generation Highly Efficient GEO Antenna in Additive Manufacturing," *IEEE Open J. Antennas Propag.*, vol. 3, pp. 69-82, 2022.

[46] C. Stoumpos, J. -A. Duran-Venegas, T. Pierré and M. García-Vigueras, "Orthomode Transducers in Additive Manufacturing for Broadband and High-Power Applications," *Proc. 17th Eur. Conf. Antennas Propag. (EuCAP'23)*, pp. 1-5, Mar. 2023.

[47] C. Stoumpos, "Design of Additive Manufacturing Oriented Top-/Narrow-Wall Couplers and 4×4 Butler Matrices," *Proc. 17th Eur. Conf. Antennas Propag. (EuCAP'23)*, pp. 1-5, Mar. 2023.

[48] http://www.3d-metalprint.com/

[49] https://www.mvg-world.com/media/1431/download/reference

[50] C. Stoumpos, T. L. Gouguec, R. Allanic, M. García-Vigueras and A. -C. Amiaud, "Compact Additively Manufactured Conformal Slotted Waveguide Antenna Array," *Antennas Wireless Propag. Lett.*, vol. 22, no. 8, pp. 1843-1847, Aug. 2023.

[51] C. Stoumpos *et al.*, "On the Additive Manufacturing of Conformal Slotted Waveguide Antennas," *Proc. 12th Int. Conf. Modern Circuits Syst. Technol. (MOCAST)*, pp. 1-4, June 2023.

[52] Calignano, F. *et al.*: "Influence of process parameters on surface roughness of aluminum parts produced by DMLS", *Int. J. Adv. Manuf. Technol.*, 2013, 67, pp. 2743–2751.

[53] K. Kamarudin, M. S. Wahab, Z. Shayfull, A. Ahmed and A. A. Raus, "Dimensional Accuracy and Surface Roughness Analysis for AlSi10Mg Produced by Selective Laser Melting (SLM)", *MATEC Web Conf.*, vol. 78, pp. 1-8, Oct. 2016.
[54] A. Maamoun, Y. Xue, M. Elbestawi and S. Veldhuis, "Effect of Selective Laser Melting Process Parameters on the Quality of Al Alloy Parts: Powder Characterization, Density, Surface Roughness, and Dimensional Accuracy," *Materials*, vol. 11, no. 12, p. 2343, Nov. 2018.
[55] O. Paverini *et al.*, "Additive manufacturing of Ku/K-band waveguide filters: a comparative analysis among selective-laser melting and stereolithography," *IET Microw. Antennas Propag.*, vol. 11, no. 14, pp. 1936-1942, Nov. 2017.
[56] O. Paverini *et al.*, "Selective Laser Melting Manufacturing of Microwave Waveguide Devices," *Proc. IEEE*, vol. 105, no. 4, pp. 620-631, Apr. 2017.

Stoumpos Charalampos was born in Thessaloniki, Greece. He received the Diploma and M.Sc. degrees (Hons.) in electrical and computer engineering from the Democritus University of Thrace, Xanthi, Greece, in 2015 and 2017, respectively, and the Ph.D. degree from the Heriot-Watt University, Edinburgh, U.K, in 2020.

His PhD was part of the European Union's Horizon 2020 research and innovation program REVOLVE in partnership with Thales Alenia Space, Toulouse, France, where he spent two years as a Research Fellow in the Department of Research and Technology. From February 2021 to August 2023, he was a Post-Doctoral Fellow with the Institute National des Sciences Apliquées de Rennes (INSA Rennes), Rennes, France. His Post-Doc was funded by the Key Technology Domain (KTD) of Thales Group and he spent two years as a Research Fellow in the Department of Research and Technology and the Antennas Product Line at Thales Alenia Space, Toulouse, France. He is currently an R&D Antenna Engineer at ANYWAVES, Toulouse, France. His current research interests include microwave components, high aperture efficiency antennas, frequency selective surfaces and additive manufacturing.

Dr. Stoumpos was a recipient of the Best PhD 2022 Prize from Thales Group.

Lucas Polo-López received the B.Sc., M.Sc., and Ph.D. degrees in telecommunication engineering from the Universidad Autónoma de Madrid (UAM), Madrid, Spain, in 2014, 2016, and 2020, respectively.

He began collaborating with the Radio Frequency Circuits, Antennas and Systems (RFCAS) Group, UAM, in 2014, while he was doing his B.Sc. thesis. Since 2021, he has been a Post-Doctoral Fellow with the Institut d'Électronique et des Technologies du numéRique (IETR), Institut National des Sciences Appliquées de Rennes (INSA Rennes), Rennes, France. His current research interests include conception of novel antenna arrays and its modeling by means of hybrid simulation techniques and the application of additive manufacturing techniques to the construction of antennas and waveguide devices.

Dr. Polo-López was a recipient of two Best Ph.D. Thesis Awards, one from COIT/AEIT and other from UAM, Spain, in 2021.

Hervé Legay received the Electrical Engineering and Ph.D. degrees from the National Institute of Applied Sciences, Rennes, France, in 1988 and 1991, respectively.

Then, he was a Post-Doctoral Fellow with the University of Manitoba, Winnipeg, MB, Canada. In 1994, he joined Alcatel Space (now Thales Alenia Space), Toulouse, France. He initially conducted studies in areas of military telecommunication satellite antennas and antenna processing. He designed the architecture and the antijamming process of the first space active antenna (Syracuse 3 Program). He is currently the Head of Research on space antennas, developing disruptive antenna concepts with emerging technologies, and associated systems in telecommunication and navigation. He is also the Co-Director of the joint laboratory MERLIN, involving Thales Alenia Space, and the Institut d'Electronique et de Télécommunication de Rennes, Rennes. He is the Chair of the Group of Antenna Experts at Thales Group. He coordinates collaborations with academic and research partners. He has authored 46 patents. He conducted major developments on reflectarrays, full metal radio frequency (RF) metasurfaces, integrated and low-profile antennas, and multiple beam quasi-optical beamformers. His research interests include innovative active antenna architectures and system activities related to the monitoring of active antennas.

Dr. Legay was a Co-Prize Winner of the 2007 Schelkunoff Prize Paper Award. He was a recipient of the Gold Thales Awards in 2008, a reward for the best innovations in the Thales Group.

Thierry Pierré joined Alcatel Space (now Thales Alenia Space) at Cannes in 1998, then Toulouse (France). He received his Master's degree in mechanical engineering from the ICAM Institute, Toulouse, France in 2012.

After 14 years as a mechanical engineer at Thales Alenia Space, in 2014 he was selected for a seconded position at the Technology Research Institute (IRT) Saint Exupéry in Toulouse as a Research Engineer. In the IRT, he conducted multiple studies in the areas of material engineering and surface treatment and co-directed a thesis on polymer metal coating. Back in Thales Alenia Space, he is currently the technical manager for additive manufacturing in Toulouse. His duties include the management of qualification and industrialization activities of structural and RF parts produced through additive manufacturing. He is also co-animator of a community of material experts at COMET by CNES.

María García-Vigueras (Member, IEEE) was born in Murcia, Spain. She received the M.Sc. degree in telecommunications engineering and the Ph.D. degree from the Technical University of Cartagena, Cartagena, Spain, in 2007 and 2012, respectively.

From 2012 to 2015, she was a Research Fellow with the Laboratory of Electromagnetism and Antennas, École Polytechnique Fédérale de Lausanne, Lausanne, Switzerland. She is currently an Assistant Professor with the Institute National des Sciences Apliquées de Rennes, Rennes, France. She has coauthored more than 30 IEEE journals and 50 publications in international conferences. Her current research interests include leaky wave antennas, periodic surfaces, active antennas, waveguide feed chain components, and the evaluation of additive manufacturing's potential for RF design.

Dr. García-Vigueras is also a Junior Member of Institute Universitaire de France (IUF) (2023–2028) with the Innovation Chair. Since 2021, she has been the Co-Chair of the EurAAP working group Women in Antennas and Propagation (WiAP). She was a recipient of several prizes, including two best Ph.D. thesis awards from COIT/AEIT, in 2014, and UPTC, Spain, in 2013, respectively, the best paper awards in MAPE 2013 in Chengdu, China, EuCAP 2012 in Prague, Czech Republic, and the EuMA Roberto Sorrentino Prize, in 2023, in the European Microwave Week in Berlin, Germany.